Galaxy clusters at $z \sim 1$ imaged by ALMA with the Sunyaev–Zel'dovich effect

Tetsu K**ITAYAMA** [ID],[1,*] **Shutaro** U**EDA** [ID],[2,3] **Nobuhiro** O**KABE** [ID],[4,5,6,7]
Takuya A**KAHORI** [ID],[8,9] **Matt** H**ILTON** [ID],[10,11,12] **John P.** H**UGHES** [ID],[13]
Yuto I**CHINOHE** [ID],[14] **Kotaro** K**OHNO** [ID],[15,16] **Eiichiro** K**OMATSU** [ID],[17,18]
Yen-Ting L**IN** [ID],[2] **Hironao** M**IYATAKE** [ID],[18,19,20,21,22] **Masamune** O**GURI** [ID],[23,24]
Cristóbal S**IFÓN** [ID],[25] **Shigehisa** T**AKAKUWA** [ID],[2,26] **Motokazu** T**AKIZAWA** [ID],[27]
Takahiro T**SUTSUMI** [ID],[28] **Joshiwa** VAN **M**ARREWIJK [ID],[29]
and **Edward J.** W**OLLACK** [ID][30]

[1]Department of Physics, Toho University, 2-2-1 Miyama, Funabashi, Chiba 274-8510, Japan
[2]Academia Sinica Institute of Astronomy and Astrophysics (ASIAA), No. 1, Section 4, Roosevelt Road, Taipei 10617, Taiwan
[3]Institute of Astronomy, National Tsing Hua University, Hsinchu 30013, Taiwan
[4]Department of Physics, Hiroshima University, 1-3-1 Kagamiyama, Higashi-Hiroshima, Hiroshima 739-8526, Japan
[5]Astrophysical Science Center, Hiroshima University, 1-3-1 Kagamiyama, Higashi-Hiroshima, Hiroshima 739-8526, Japan
[6]Core Research for Energetic Universe, Department of Physics, Hiroshima University, 1-3-1 Kagamiyama, Higashi-Hiroshima, Hiroshima 739-8526, Japan
[7]Physics Program, Graduate School of Advanced Science and Engineering, Hiroshima University, 1-3-1 Kagamiyama, Higashi-Hiroshima, Hiroshima 739-8526, Japan
[8]Mizusawa VLBI observatory, National Astronomical Observatory of Japan, 2-21-1 Osawa, Mitaka, Tokyo 181-8588, Japan
[9]Operation Division, SKA Observatory, Jodrell Bank, Lower Withington, Macclesfield SK11 9DL, UK
[10]Astrophysics Research Centre, University of KwaZulu-Natal, Westville Campus, Durban 4041, South Africa
[11]School of Mathematics, Statistics & Computer Science, University of KwaZulu-Natal, Westville Campus, Durban 4041, South Africa
[12]Wits Centre for Astrophysics, School of Physics, University of the Witwatersrand, Private Bag 3, Johannesburg 2050, South Africa
[13]Department of Physics and Astronomy, Rutgers, The State University of New Jersey, Piscataway, NJ 08854-8019, USA
[14]Department of Physics, Rikkyo University, 3-34-1 Nishi-Ikebukuro, Toshima-ku, Tokyo 171-8501, Japan
[15]Institute of Astronomy, School of Science, The University of Tokyo, 2-21-1 Osawa, Mitaka, Tokyo 181-0015, Japan
[16]Research Center for the Early Universe, School of Science, The University of Tokyo, 7-3-1 Hongo, Bunkyo, Tokyo 113-0033, Japan
[17]Max-Planck-Institut für Astrophysik, Karl-Schwarzschild Str. 1, D-85741 Garching, Germany
[18]Kavli Institute for the Physics and Mathematics of the Universe (Kavli IPMU, WPI), The University of Tokyo Institutes for Advanced Study, The University of Tokyo, 5-1-5 Kashiwanoha, Kashiwa, Chiba 277-8583, Japan

[19]Kobayashi-Maskawa Institute for the Origin of Particles and the Universe (KMI), Nagoya University, Furo-cho, Chikusa-ku, Nagoya, Aichi 464-8602, Japan

[20]Institute for Advanced Research, Nagoya University, Furo-cho, Chikusa-ku, Nagoya, Aichi 464-8601, Japan

[21]Division of Particle and Astrophysical Science, Graduate School of Science, Nagoya University, Furo-cho, Chikusa-ku, Nagoya, Aichi 464-8602, Japan

[22]Jet Propulsion Laboratory, California Institute of Technology, Pasadena, CA 91109, USA

[23]Center for Frontier Science, Chiba University, 1-33 Yayoi-cho, Inage-ku, Chiba, Chiba 263-8522, Japan

[24]Department of Physics, Graduate School of Science, Chiba University, 1-33 Yayoi-Cho, Inage-Ku, Chiba, Chiba 263-8522, Japan

[25]Instituto de Física, Pontificia Universidad Católica de Valparaíso, Casilla 4059, Valparaíso, Chile

[26]Department of Physics and Astronomy, Graduate School of Science and Engineering, Kagoshima University, 1-21-35 Korimoto, Kagoshima, Kagoshima 890-0065, Japan

[27]Department of Physics, Yamagata University, 1-4-12 Kojirakawa-machi, Yamagata, Yamagata 990-8560, Japan

[28]National Radio Astronomy Observatory, PO Box O, Socorro, NM 87801, USA

[29]European Southern Observatory (ESO), Karl-Schwarzschild-Str. 2, Garching D-85748, Germany

[30]NASA/Goddard Space Flight Center, Greenbelt, MD 20771, USA

*E-mail: kitayama@ph.sci.toho-u.ac.jp

Abstract

We present high angular resolution measurements of the thermal Sunyaev–Zel'dovich effect (SZE) toward two galaxy clusters, RCS J2319+0038 at $z = 0.9$ and HSC J0947−0119 at $z = 1.1$, by the Atacama Large Millimeter/submillimeter Array (ALMA) in Band 3. They are supplemented with available Chandra X-ray data, optical data taken by Hyper Suprime-Cam on Subaru, and millimeter-wave SZE data from the Atacama Cosmology Telescope. Taking into account departures from spherical symmetry, we have reconstructed non-parametrically the inner pressure profile of two clusters as well as electron temperature and density profiles for RCS J2319+0038. This is one of the first such measurements for an individual cluster at $z \gtrsim 0.9$. We find that the inner pressure profile of both clusters is much shallower than that of local cool-core clusters. Our results consistently suggest that RCS J2319+0038 hosts a weak cool core, where radiative cooling is less significant than in local cool cores. On the other hand, HSC J0947−0119 exhibits an even shallower pressure profile than RCS J2319+0038 and is more likely to be a non-cool-core cluster. The SZE centroid position is offset by more than 140 h_{70}^{-1} kpc from the peaks of galaxy distribution in HSC J0947−0119, suggesting a stronger influence of mergers in this cluster. We conclude that these distant clusters are at a very early stage of developing the cool cores typically found in clusters at lower redshifts.

Key words: cosmology: observations — galaxies: clusters: intracluster medium — galaxies: clusters: individual (RCS J2319+0038, HSC J0947−0119) — radio continuum: galaxies — techniques: interferometric

1 Introduction

The baryonic content of galaxy clusters is dominated by hot ($\gtrsim 10^7$ K) and tenuous ($\lesssim 0.1$ cm^{-3}) plasma, referred to as the intracluster medium (ICM). The ICM properties of nearby ($z \lesssim 0.2$) clusters are well studied thanks to resolved measurements of X-ray surface brightness and temperature profiles from a large number of clusters (see, e.g., Böhringer & Werner 2010; Cavaliere & Lapi 2013 for reviews). Such profiles encode the thermodynamic evolution of clusters driven by mergers, accretion, and AGN

feedback on one hand and radiative cooling on the other. It is recognized that there is a wide diversity in the properties of central cores ($\lesssim 100$ kpc), within which cooling and feedback processes play important roles in sculpting their thermodynamic properties. Broadly speaking, galaxy clusters are divided into two groups: "cool-core" and "non-cool-core" clusters (e.g., Peres et al. 1998; Bauer et al. 2005). The former group is also characterized as having peaked or cuspy gas density profiles, whereas the latter often shows clear signs of disturbance.

At $z \gtrsim 1$, the observational situation is much less certain. There are only a handful of galaxy clusters whose thermodynamic structure has been studied at these redshifts in X-rays (Santos et al. 2012; McDonald et al. 2014; Tozzi et al. 2015; Brodwin et al. 2016; Bartalucci et al. 2017; Sanders et al. 2018; Mantz et al. 2020; Ghirardini et al. 2021). This is mainly because the observed X-ray surface brightness decreases as $\propto (1 + z)^{-4}$ and the observed sizes of clusters become small (e.g., a typical core radius of 100 kpc corresponds to $\sim 12''$ at $z \gtrsim 1$, whereas the half-energy width of XMM–Newton is $\sim 15''$). As a result, it is very challenging to measure spatially resolved temperature structures from X-ray spectral analyses. Efforts to measure thermodynamic profiles at high z often employ stacking methods to obtain average profiles for samples of clusters observed over broad redshift ranges, e.g., $0.6 < z < 1.2$ (McDonald et al. 2014).

In this regard, the Sunyaev–Zel'dovich effect (SZE; Sunyaev & Zeldovich 1970, 1972) serves as a useful probe of distant galaxy clusters (see Mroczkowski et al. 2019 for a recent review). For given electron density n_e and temperature T_e, the surface brightness of the SZE is proportional to $n_e T_e$, whereas that of X-rays varies as $n_e^2 \Lambda(T_e)(1 + z)^{-4}$, where Λ is typically a weak function of T_e. The SZE brightness is free from the aforementioned $(1 + z)^{-4}$ dimming and provides a direct measure of electron thermal pressure. The advent of large-area SZE surveys by the South Pole Telescope (SPT; e.g., Staniszewski et al. 2009; Vanderlinde et al. 2010; Williamson et al. 2011; Reichardt et al. 2013; Bleem et al. 2015; Huang et al. 2020) and the Atacama Cosmology Telescope (ACT; e.g., Hincks et al. 2010; Marriage et al. 2011; Hasselfield et al. 2013; Hilton et al. 2018, 2021) has significantly increased the number of galaxy clusters detected at $z \gtrsim 1$. Resolved SZE images of clusters at $z \gtrsim 1$ with an angular resolution of $<20''$ have been obtained by MUSTANG on the Green Bank Telescope (Korngut et al. 2011; Dicker et al. 2020; Andreon et al. 2021), NIKA on the IRAM telescope (Adam et al. 2015, 2018), and the Atacama Large Millimeter/submillimeter Array (ALMA) (Basu et al. 2016; Gobat et al. 2019; Di Mascolo et al. 2020, 2021).

In this paper, we present high angular resolution SZE images of galaxy clusters, RCS J2319+0038 at $z = 0.90$ and HSC J0947−0119 at $z = 1.11$, taken by ALMA, and supplement them with available X-ray, optical, and wider-field SZE data. Because of their much smaller mass, the SZE signal of RCS J2319+0038 and HSC J0947−0119 is weaker, by a factor of up to 5, than that of massive galaxy clusters at lower redshifts studied by ALMA previously, e.g., RX J1347.5−1145 at $z = 0.45$ and SPT-CL J2334−4243 at $z = 0.60$ (Kitayama et al. 2016, 2020). The present paper therefore makes use of some of the deepest ALMA SZE data obtained so far. Our goal is to reveal thermodynamic structures of clusters at $z \sim 1$ in conjunction with galaxy distributions, and weak lensing mass maps. We develop a method to reconstruct electron pressure and temperature profiles of distant clusters non-parametrically, taking into account departures from spherical symmetry. We also include or clarify various systematic effects associated with the analysis.

RCS J2319+0038 is the most massive galaxy cluster in a spectroscopically confirmed supercluster at $z \sim 0.9$ (Gilbank et al. 2008), discovered by the Red-Sequence Cluster Survey (RCS; Gladders & Yee 2005). We adopt for this cluster the spectroscopic redshift of $z = 0.90$ from Gilbank et al. (2008). Based on the X-ray observation with Chandra (Hicks et al. 2008), the density profile of the ICM is well constrained, whereas only the average spectroscopic temperature is measured owing to the large distance to the cluster. More recently, RCS J2319+0038 was also detected in the ACT Data Release 5 (DR5; Naess et al. 2020) cluster search[1] (Hilton et al. 2021), with a signal-to-noise ratio (S/N) of 5.2. We note that the centroid position of the ACT SZE signal is offset from the X-ray peak by $\sim 30''$. We will explore the origin of this offset by means of higher angular resolution SZE data.

HSC J0947−0119 was discovered more recently by the Hyper Suprime-Cam Subaru Strategic Program (HSC-SSP; Miyazaki et al. 2018; Komiyama et al. 2018; Furusawa et al. 2018; Bosch et al. 2018; Huang et al. 2018; Coupon et al. 2018; Tanaka et al. 2018; Aihara et al. 2018a, 2018b, 2019) using the Cluster finding Algorithm based on Multi-band Identification of Red-sequence gAlaxies (CAMIRA; Oguri 2014; Oguri et al. 2018). Given the lack of accurate spectroscopic measurements, we adopt for this cluster the photometric redshift[2] of $z = 1.11$ from the CAMIRA

---

[1] ⟨https://lambda.gsfc.nasa.gov/product/act/actadv_prod_table.html⟩.

[2] $z = 1.11$ is consistent with the spectroscopic redshift obtained for several members from Magellan/LDSS3; however, our observations also suggest possible galaxy concentrations along the line of sight; we are in the process of obtaining more spectroscopic redshifts in this field.

Table 1. Summary of ALMA observations.

	RCS J2319+0038		HSC J0947−0119	
	12 m	7 m	12 m	7 m
Project code	2019.1.00673.S		2018.1.00680.S	
Field center	$(23^h19^m53\overset{s}{.}280, 0°38'13\overset{''}{.}400)$		$(9^h47^m58\overset{s}{.}565, -1°20'05\overset{''}{.}780)$	
Number of pointings	7	7	7	7
Observation start	2019 Nov 15	2019 Oct 22	2019 Jan 14	2018 Nov 28
Observation end	2019 Nov 22	2020 Jan 2	2019 Jan 20	2019 May 13
Total on-source time [h]	12.1	78.6	8.0	64.5
Number of antennas	43–47	9–11	46–51	9–12
Central frequency [GHz]	92	92	92	92
Band widths [GHz]	7.5	7.5	7.5	7.5
Baseline coverage [kλ]	4.2–147	2.5–16.3	4.2–120	2.5–16.3

catalogue for the third public data release of HSC-SSP.[3] The accuracy of the photometric redshift in this catalogue is estimated to be $\sigma_z \sim 0.01(1 + z)$ (Oguri et al. 2018). The observed richness of HSC J0947−0119 is one of the highest among the clusters at $z > 1$ identified by CAMIRA. HSC J0947−0119 is also detected in ACT DR5 with $S/N = 13.2$ (Hilton et al. 2021), which is among the highest-significance SZE detection at $z > 1$ by ACT. At the time of writing, deep X-ray observations for this cluster are unavailable.

Throughout the paper, we adopt a standard set of cosmological density parameters, $\Omega_M = 0.3$ and $\Omega_\Lambda = 0.7$. We use the dimensionless Hubble constant $h_{70} \equiv H_0/(70\,\mathrm{km\,s^{-1}\,Mpc^{-1}})$; given existing tensions in the value of H_0 (e.g., Verde et al. 2019) the parameter is unconstrained unless otherwise indicated. In this cosmology, an angular size of $1''$ corresponds to physical sizes of $7.79\,h_{70}^{-1}$ kpc and $8.19\,h_{70}^{-1}$ kpc at $z = 0.90$ and $z = 1.11$, respectively. These physical sizes are insensitive to the values of density parameters and reduce by 1.1% and 1.2% at $z = 0.90$ and $z = 1.11$, respectively, if $\Omega_M = 0.32$ and $\Omega_\Lambda = 0.68$ are adopted instead. Unless otherwise stated, the errors are given in 1σ and the coordinates are given in J2000.0.

2 Data and analysis

2.1 Millimeter: ALMA Band 3

RCS J2319+0038 and HSC J0947−0119 were observed by the 12 m and 7 m arrays of ALMA in Band 3 (project codes 2019.1.00673.S and 2018.1.00680.S) as summarized in table 1. The target fields, centered at $(23^h19^m53\overset{s}{.}280, 0°38'13\overset{''}{.}400)$ and $(9^h47^m58\overset{s}{.}565, -1°20'05\overset{''}{.}780)$ for RCS J2319+0038 and HSC J0947−0119, respectively, have diameters of about

$1'.5$ covered with one central and six surrounding hexagonal mosaic pointings by both arrays. An equal spacing of $34''.2$ between the pointings was adopted, yielding approximately a Nyquist sampling for the 12 m array and much denser sampling for the 7 m array.

The observations were executed over the periods listed in table 1, during which the number of antennas varied slightly. All the data were taken at four continuum bands centered at 85, 87, 97, and 99 GHz, yielding an overall central frequency of 92 GHz ($\lambda = 3.3$ mm) with an effective bandwidth of 7.5 GHz. The most compact configuration for the 12 m array, C1, was adopted to cover the overall baseline ranges of 2.5–147 kλ and 2.5–120 kλ for RCS J2319+0038 and HSC J0947−0119, respectively, where λ is the observed wavelength.

For both objects, we used the visibility data produced by the second stage of ALMA's Quality Assurance process (QA2). Imaging was done with the Common Astronomy Software Applications package (CASA) (McMullin et al. 2007; CASA Team 2022) version 6.4.0. The procedure was similar to that adopted by Kitayama et al. (2016, 2020). First, we identified compact sources in the observing field using only the baselines longer than 15 kλ; the position and the flux density were determined in the *uv* plane by the CASA task *uvmodelfit*. To improve the signal-to-noise ratio, all spectral channels were fitted together,[4] excluding the frequency ranges affected by line emissions; separation of line emissions is described in the Appendix. All the compact sources detected at $>5\sigma$ (tables 3 and 4) were subtracted from all of the visibility data. Secondly, we performed image deconvolution with the Multi-Scale CLEAN algorithm (Cornwell 2008; Rich et al. 2008; J.-W. Steeb

---

4 We checked that this simplification has no apparent effect on the results of the present paper. For the brightest source (C1 in table 3), adopting the flux density fitted separately at 85, 87, 97, and 99 GHz for subtraction would change the residual signal at the source position by less than 1/5 of the noise level.

Table 2. Properties of the synthesized images from a range of baselines.

	RCS J2319+0038				HSC J0947−0119			
	>15kλ	12 m	7 m	All*	>15kλ	12 m	7 m	All*
Beam major axis FWHM [″]	3.14	3.60	18.7	3.76	3.16	3.63	17.8	3.77
Beam minor axis FWHM [″]	2.82	3.25	11.9	3.38	2.71	3.11	11.2	3.22
Beam position angle [°]	82.2	82.6	−86.1	82.5	−90.0	−89.1	−84.4	−89.1
Average 1σ noise [μJy beam^{-1}]	5.6	5.0	19.4	4.8	5.8	5.1	21.0	5.0

*The 1σ noise for all baselines after smoothing to 5″ FWHM is 5.8 μJy beam^{-1} and 5.9 μJy beam^{-1} for RCS J2319+0038 and HSC J0947−0119, respectively.

Table 3. Positions and continuum flux densities of point sources toward RCS J2319+0038 obtained with the CASA task *uvmodelfit*.*

Source ID	RA (J2000.0)	Dec (J2000.0)	92 GHz flux density [μJy]
C1	$23^{h}19^{m}53\overset{s}{.}32$	$0°38'16\overset{''}{.}52$	262.9 ± 3.9
C2	$23^{h}19^{m}53\overset{s}{.}41$	$0°38'13\overset{''}{.}83$	36.6 ± 3.9
W[†]	$23^{h}19^{m}49\overset{s}{.}70$	$0°37'56\overset{''}{.}48$	76.8 ± 6.1

*The errors in the positions are less than $0\overset{''}{.}2$.

[†]For source W, the frequency ranges affected by line emissions (table 10) are excluded in the fit.

Table 4. Same as table 3, but for HSC J0947−0119.

Source ID	RA (J2000.0)	Dec (J2000.0)	92 GHz flux density [μJy]
W1*	$9^{h}47^{m}55\overset{s}{.}46$	$-1°20'26\overset{''}{.}98$	35.3 ± 4.9
W2	$9^{h}47^{m}57\overset{s}{.}50$	$-1°19'51\overset{''}{.}77$	42.2 ± 4.5

*For source W1, the frequency range affected by a line emission (table 10) is excluded in the fit.

& U. Rau 2019[5]) using the CASA task *tclean*. Given similar sensitivity and source size between RCS J2319+0038 and HSC J0947−0119, we adopted a circular mask region with a radius 50″ and a flux threshold of 0.01 mJy (corresponding to $\sim 2\sigma$) for both objects. The choices of the other parameters were identical to Kitayama et al. (2020); we adopted [0, 4″, 8″, 16″, 32″, 64″] as the FWHMs of the Gaussian components, the multi-frequency synthesis mode in joint mosaic imaging, and natural weighting. All the ALMA images presented in this paper are corrected for primary beam attenuation (e.g., Mason 2020) and have a pixel size of $0\overset{''}{.}5$.

Table 2 lists the parameters of the synthesized beams as well as the 1σ noise levels of the synthesized image within 45″ from the field center. To eliminate large-scale variation of the data caused by the SZE, the noise levels were measured on difference maps created after subtracting the compact sources (tables 3 and 4); the visibility data were divided into the first and second halves along the time sequence of observations, the sign of the latter was flipped, concatenated with the former, and the result was inverse Fourier transformed into the image domain.

For display purposes, we also present the images smoothed by a Gaussian filter to an effective beam size of 5″ FWHM. The root-mean-square (RMS) noise level measured on the above-mentioned difference map smoothed to

[5] Steeb, J.-W., & Rau, U. 2019, CASA Memo No. 9 ⟨https://casadocs.readthedocs.io/⟩.

the 5″ resolution is 5.8 μJy beam^{-1} and 5.9 μJy beam^{-1} for RCS J2319+0038 and HSC J0947−0119, respectively. These RMS values are only used for characterizing the significance levels of the SZE signal on the smoothed images. Unless otherwise stated, quantitative analysis in this paper is done on the unsmoothed images created from all baselines whose characteristics are listed in table 2.

2.2 Millimeter: ACT

We extracted the ACT DR5 data of RCS J2319+0038 and HSC J0947−0119. The ACT DR5 cluster search used the 98, 150 GHz maps made from all ACT data obtained between 2008 and 2018, including both day and night time observations (see Naess et al. 2020 for details of the data products used). The approximate beam FWHMs are $2\overset{'}{.}2$ and $1\overset{'}{.}4$ at 98 GHz and 150 GHz, respectively. The S/N of the ACT maps presented in this paper is measured at a fixed filter scale of $2\overset{'}{.}4$ as described in Hilton et al. (2021).

2.3 X-ray: Chandra ACIS-S

Of the two clusters studied in this paper, deep X-ray data are available only for RCS J2319+0038. We extracted four datasets taken in 2005 by Chandra ACIS-S for this cluster (ObsID: 5750, 7172, 7173, and 7174). After excluding the periods with high background rates, the total net exposure time is 69.7 ks. The data were processed with CIAO version 4.13 (Fruscione et al. 2006) and the Calibration database (CALDB) version 4.9.6. The backgrounds were estimated from the off-center region at $\theta > 3\overset{'}{.}2$ from the emission peak of this cluster, where the ICM

emission is negligible. Exposure-corrected and background-subtracted data at observed energies $E_{obs} = 0.4$–7.0 keV were used throughout our analysis; for display purposes only, we applied adaptive smoothing to the brightness image including backgrounds using the task *fadapt* implemented in FTOOLS[6] (Blackburn 1995; Blackburn et al. 1999; NASA High Energy Astrophysics Science Archive Research Center (Heasarc) 2014). Spectral fitting was done with XSPEC version 12.12.0 (Arnaud 1996), assuming that the ICM is in collisional ionization equilibrium and the metal abundance Z is 0.3 times the solar value given by Anders and Grevesse (1989). The source redshift and the Galactic hydrogen column density were fixed at $z = 0.90$ and $N_H = 4.2 \times 10^{20}$ cm^{-2} (HI4PI Collaboration 2016), respectively. We fixed the helium mass fraction at $Y = 0.25$, which is nearly unchanged between the primordial gas and the solar photosphere (e.g., Asplund et al. 2009; Planck Collaboration 2020).

2.4 Optical: Subaru Hyper Suprime-Cam

RCS J2319+0038 and HSC J0947−0119 were both observed by five broad-band filters *grizy* (Kawanomoto et al. 2018) in the HSC-SSP. We used the CAMIRA cluster catalogue (Oguri et al. 2018) updated for the third public data release of HSC-SSP (Aihara et al. 2022) based on the associated bright star masks (Coupon et al. 2018).

Weak lensing analysis was done on the HSC-SSP S19A data,[7] following the method described in Okabe et al. (2019, 2021). The galaxy shapes were measured using the re-Gaussianization method (Hirata & Seljak 2003) implemented in the HSC pipeline (Mandelbaum et al. 2018; Li et al. 2022). The background galaxies behind each cluster were selected using the color–color selection following Medezinski et al. (2018). The S/N of the resulting surface mass density is computed as in Okabe et al. (2019). We adopted the NFW density profile (Navarro et al. 1996) for estimating the deprojected halo mass from the tangential shear profiles; given the low S/N ($\sim$2–3) of the lensing signal, the halo concentration is linked to the mass by the relation of Diemer and Kravtsov (2015).

3 Results

3.1 Compact millimeter sources

3.1.1 RCS J2319+0038
There are three compact sources above the 5σ significance level at 92 GHz in our target field toward RCS J2319+0038

as shown in figures 1a–1d. Only compact sources, not the SZE, are visible on the images from long baselines. All the detected sources are consistent with being point-like and their properties are summarized in table 3.

Two sources (C1 and C2) are located within $5''$ from the X-ray center of RCS J2319+0038. There is a galaxy detected by HSC at the photometric redshift of $z_{phot} = 0.92 \pm 0.04$ within $0\rlap{.}''2$ from C1. Two galaxies at $z_{phot} = 0.91 \pm 0.03$ and 0.92 ± 0.02 lie at the projected distance of $0\rlap{.}''6$ from C2; the latter is the brightest cluster galaxy (BCG) of RCS J2319+0038. Both C1 and C2 are bright at lower frequencies and detected in the Faint Images of the Radio Sky at Twenty-cm (FIRST; Becker et al. 1995) as well as the Very Large Array Sky Survey (VLASS; Gordon et al. 2021). Their combined flux listed in the FIRST Catalog Database[8] is 4.59 ± 0.22 mJy at 1.4 GHz, where we have estimated the error from the image of this region available at the FIRST Cutout Server.[9] The flux measured on the VLASS Epoch 1.1 image[10] within a diameter of $15''$ around the position of C1 is 4.9 ± 0.5 mJy at 3.0 GHz. Figures 1a and 1b indicate that the peak intensity ratio between C1 and C2 is about 2.3 : 1 and 7.4 : 1 at 3.0 GHz and 92 GHz, respectively, implying that C2 has a much steeper spectrum than C1. Note that the dust emission can dominate the source flux at 92 GHz, corresponding to the rest-frame frequency of 175 GHz at $z = 0.90$. The luminosity of C1 and C2 is $\nu L_\nu = (9.74 \pm 0.14) \times 10^{41} h_{70}^{-2}$ erg s^{-1} and $(1.36 \pm 0.14) \times 10^{41} h_{70}^{-2}$ erg s^{-1}, respectively, at $\nu = 175$ GHz in the rest-frame of the cluster.

Another source (W) is located at $\sim 1'$ from the X-ray center of RCS J2319+0038. This source hosts bright line emissions as described in the Appendix. It has no obvious optical counterpart within $1''$ and is undetected at 1.4 GHz in the FIRST and VLASS images.

The above sources are removed from the visibility data in our subsequent analysis. Figures 1d and 1e show that the residuals at long baselines are consistent with noise, whereas the extended signal from the ICM becomes apparent once shorter baselines are included.

3.1.2 HSC J0947−0119
There are two compact sources above the 5σ significance level at 92 GHz in our target field toward HSC J0947−0119 (figure 2 and table 4). All the detected sources are consistent with being point-like and removed from the visibility data in our subsequent analysis.

---

[6] ⟨https://heasarc.gsfc.nasa.gov/ftools/⟩.

[7] S19A is an internal data release between the second and third public data releases of HSC-SSP.

[8] ⟨http://sundog.stsci.edu/⟩.

[9] ⟨https://third.ucllnl.org/cgi-bin/firstcutout⟩.

[10] ⟨http://cutouts.cirada.ca/⟩.
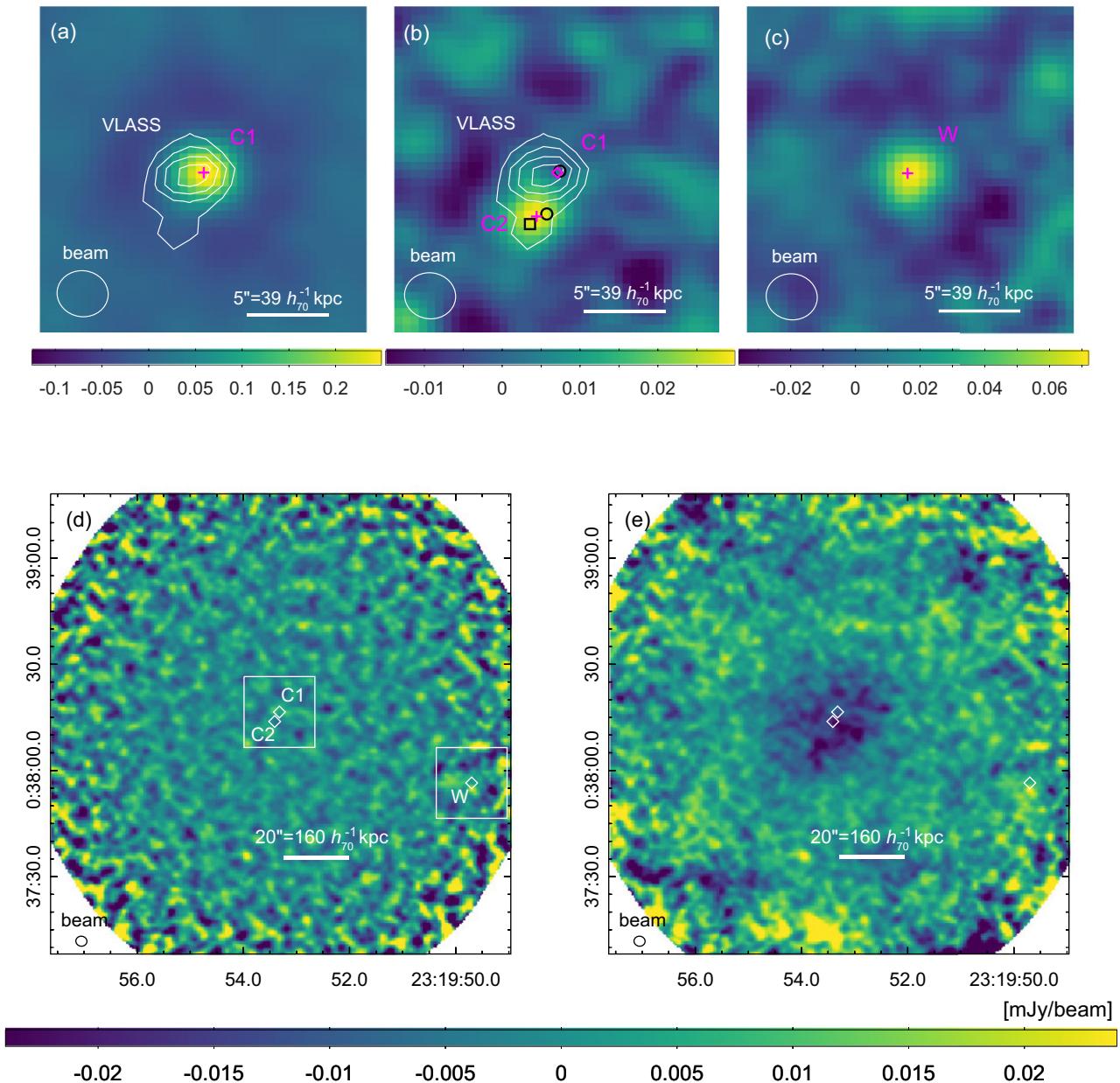
Fig. 1. Dirty maps toward RCS J2319+0038 from only long baselines at $>15k\lambda$ [panels (a)–(d)] and all baselines at $>2.5k\lambda$ [panel (e)]. The regions shown in panels (a)–(c) are indicated by boxes in panel (d). The positions of $>5\sigma$ sources before and after subtraction are marked by crosses and diamonds, respectively. The synthesized beam shape of ALMA is shown at the bottom left in each panel. (a) Central $20'' \times 20''$ region before the sources are subtracted. Contours show the 3.0 GHz intensity (90%, 70%, 50%, 30% of the peak value) from the VLASS Epoch 1.1 image with synthesized beam FWHMs of $2''.8 \times 2''.2$ and a position angle of $7°.5$. (b) Same as panel (a), but after the brightest source, C1, is subtracted. The position of an optical counterpart candidate (see text) is marked by a circle (or a box if the candidate is the BCG). (c) The region around source W. (d) Long-baseline image after sources C1, C2, and W are subtracted. (e) Similar to panel (d), but produced from all baselines.

One source (W1) lies at $\sim 1'$ south-west of the ALMA SZE center. This source appears to host a bright line emission as described in the Appendix. There is a compact object classified as a star in the SDSS Data Release 17 (Abdurro'uf et al. 2022)[11] at $0''.6$ from this source. There is no other object detected by HSC, VLASS, or FIRST within a projected distance of $1''$ from W1.

Another source (W2) is located at $\sim 20''$ north-west of the ALMA SZE center. There is a galaxy detected by HSC at a photometric redshift of $z_{phot} = 0.9 \pm 0.5$ lying at $0''.5$ from this source. It is undetected by VLASS or FIRST. The large uncertainty in z_{phot} of this object is due to degeneracy of the spectral energy distribution (SED) modeling of low-z and high-z galaxies in the five-band photometric space (Tanaka 2015).

[11] ⟨http://skyserver.sdss.org/dr17⟩.
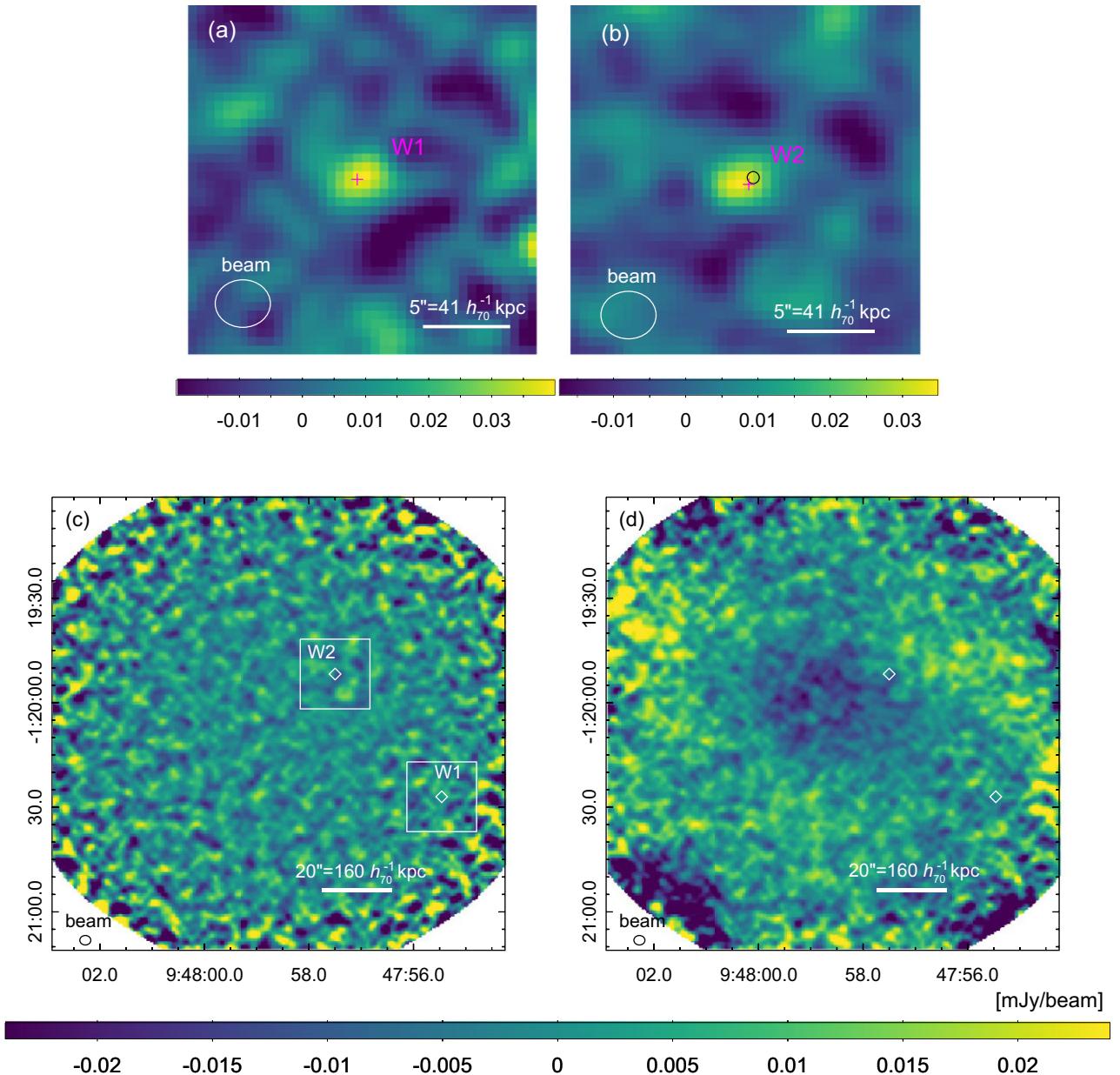
Fig. 2. Similar to figure 1 but toward HSC J0947−0119. The regions shown in panels (a) and (b) are indicated by boxes in panel (c). (a) Long-baseline ($>15\,\mathrm{k}\lambda$) image of the region around source W1. (b) Similar to panel (a), but for the region around source W2. The position of an optical counterpart candidate (see text) is marked by a circle. (c) Long-baseline image after sources W1 and W2 are subtracted. (d) Similar to panel (c), but produced from all baselines.

Figures 2c and 2d further demonstrate that the above sources are subtracted successfully and do not affect the extended signal from the ICM.

3.2 The intracluster medium

3.2.1 RCS J2319+0038

Figure 3 shows the deconvolved ALMA image of RCS J2319+0038 after the compact sources listed in

table 3 have been removed. The image has been smoothed to an effective beam size of $5''$ FWHM for display purposes. To obtain the overall morphology of the signal, we fit the unsmoothed ALMA image with an elliptical Gaussian using the CASA task *imfit*, varying its center, major and minor axis FWHMs, and the position angle[12] (table 5); errors of fitted parameters are estimated based on

---

[12] In this paper, the position angle is measured for the major axis of an ellipse from north ($0°$) through east ($90°$).
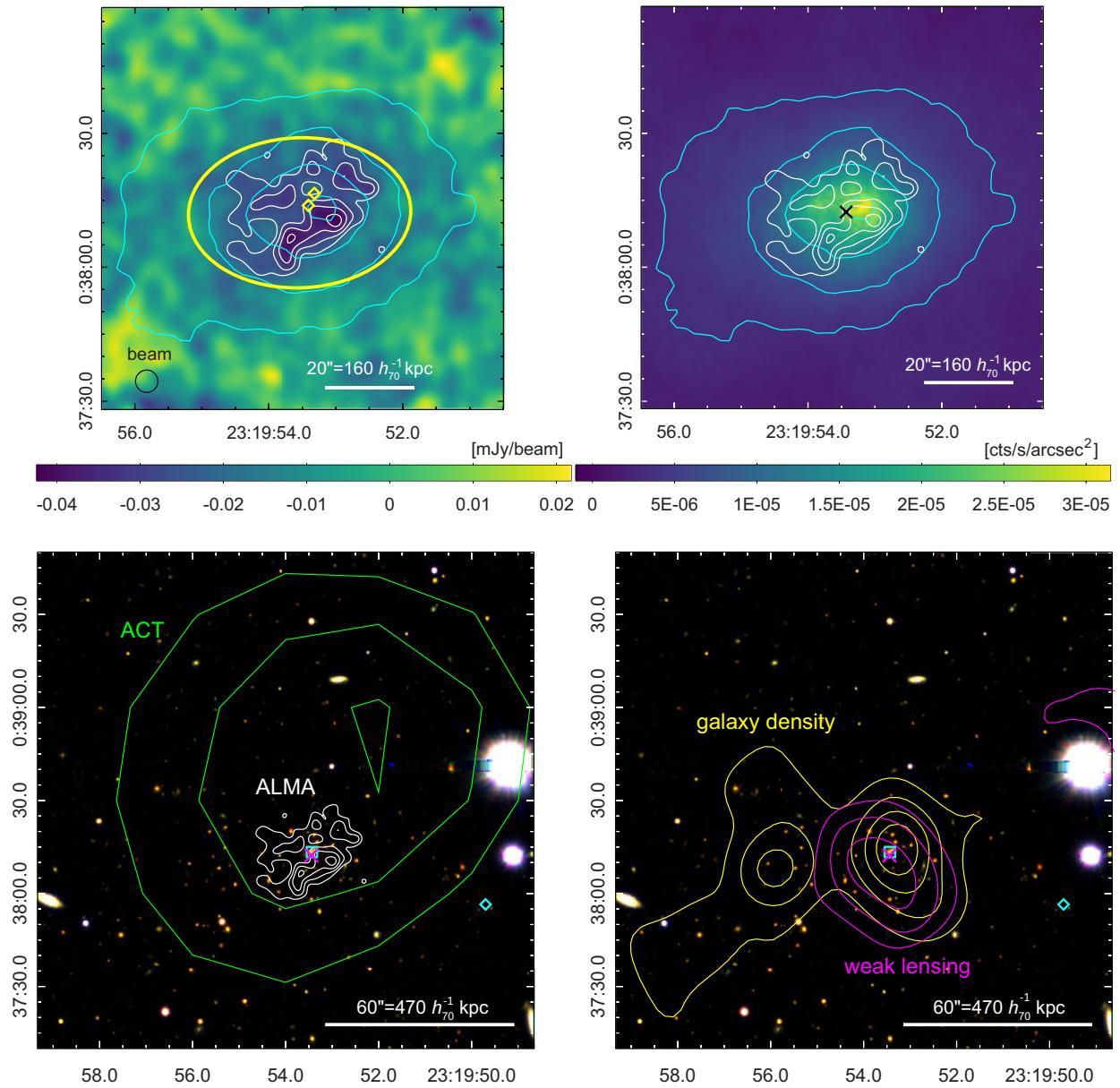
Fig. 3. Multi-wavelength view of RCS J2319+0038 at $z = 0.90$. Top left: Deconvolved ALMA SZE image at the central frequency of 92 GHz smoothed to have a beam size of 5″ FWHM. The ellipse shows the FWHM location of the best-fitting elliptical Gaussian profile (table 5), and the diamonds indicate the positions of subtracted sources. Top right: Chandra 0.4–7.0 keV X-ray brightness image adaptively smoothed with a circular top-hat filter that contains at least 100 photons. The cross marks the X-ray center defined in the text. Bottom left and bottom right: Wider-field HSC-SSP optical *riz*-color images with the X-ray center marked by a cross. The positions of the BCG and the off-center source W are indicated by a box and a diamond, respectively. Wherever plotted, white contours show the significance levels of the ALMA SZE image (4–7σ in increments of 1σ = 5.8 μJy beam^{-1}), cyan contours the brightness of the Chandra X-ray image (80%, 40%, 20%, 10% of the peak value), green contours the significance levels of the SZE map from the ACT DR5 cluster catalogue ($S/N = 3$, 4, and 5), yellow contours the surface density of probable member galaxies averaged by a Gaussian with 20″ FWHM (80%, 60%, 40%, 20% of the peak value), and magenta contours the projected weak lensing mass smoothed by a Gaussian with 30″ FWHM ($S/N = 1.5$, 2, and 2.5).

Condon (1997), assuming a constant noise level within a radius of 50″ from the field center. The extended SZE signal is detected at high significance with ALMA with a mean size of ~40″ FWHM and an axis ratio of ~0.7. The integrated flux density within a radius of 45″ from the position shown in table 5 is -1.98 ± 0.10 mJy; for

reference, the flux inferred from the elliptical Gaussian fit is -2.04 ± 0.20 mJy.

The figure also shows the Chandra X-ray brightness image of RCS J2319+0038 adaptively smoothed with a circular top-hat filter that contains at least 100 photons. We fit the unsmoothed X-ray brightness with an elliptical β model

Table 5. Results of an elliptical Gaussian fit to the ALMA image within a radius of 50″ from the field center by the CASA task *imfit*.*

	RA (J2000.0)	Dec (J2000.0)	Major axis FWHM [″]	Minor axis FWHM [″]	Position angle [°]	Flux density [mJy]
RCS J2319+0038	$23^{\rm h}19^{\rm m}53\overset{\rm s}{.}54$	$0°38′12\overset{″}{.}19$	49.8 ± 4.8	33.6 ± 3.2	92.0 ± 9.7	-2.04 ± 0.20
HSC J0947−0119	$9^{\rm h}47^{\rm m}58\overset{\rm s}{.}74$	$-1°19′58\overset{″}{.}37$	58.6 ± 3.5	38.7 ± 2.3	72.3 ± 5.5	-4.12 ± 0.24

*The errors in the central positions are less than $2\overset{″}{.}1$.

Table 6. Results of an elliptical β model fit using equations (1) and (2) to the Chandra brightness data of RCS J2319+0038 with the Sherpa package.*

x_0 (J2000.0)	y_0 (J2000.0)	S_0 [counts s^{-1} arcsec^{-2}]	β	$\theta_{\rm c}$ [″]	q	ψ [°]
$23^{\rm h}19^{\rm m}53\overset{\rm s}{.}45$	$0°38′12\overset{″}{.}29$	$(2.64^{+0.21}_{-0.20}) \times 10^{-5}$	$0.673^{+0.034}_{-0.032}$	$13.2^{+1.4}_{-1.2}$	$0.694^{+0.036}_{-0.034}$	96.7 ± 3.9

*The errors in the central positions (x_0 and y_0) are less than $0\overset{″}{.}6$.

of the form

$$S(\vec{\theta}) = S_0 \left[1 + \left(\frac{\bar{\theta}}{\theta_{\rm c}} \right)^2 \right]^{-3\beta + \frac{1}{2}}, \tag{1}$$

with the position vector on the sky $\vec{\theta} \equiv (x, y)$ related to the "circular mean distance" $\bar{\theta} \equiv \sqrt{\bar{x}^2 + \bar{y}^2}$ from the emission center (x_0, y_0) by

$$\begin{pmatrix} \bar{x} \\ \bar{y} \end{pmatrix} \equiv \begin{pmatrix} \frac{1}{\sqrt{q}} & 0 \\ 0 & \sqrt{q} \end{pmatrix} \begin{pmatrix} \cos\psi & \sin\psi \\ -\sin\psi & \cos\psi \end{pmatrix} \begin{pmatrix} x - x_0 \\ y - y_0 \end{pmatrix}, \tag{2}$$

where S_0 is the brightness at (x_0, y_0), $\theta_{\rm c}$ is the angular core radius, q is the minor-to-major axis ratio ($q \leq 1$) on the sky, ψ is the position angle, and $\bar{x}$ is intended to align with the minor axis of the ellipse. We used the Sherpa modeling package (*beta2d*) in CIAO (Freeman et al. 2001; Doe et al. 2007; Refsdal et al. 2009) for this purpose. The best-fitting values of x_0, y_0, S_0, β, $\theta_{\rm c}$, q, and ψ are listed in table 6.

The overall morphology of the SZE on the sky is in agreement with that of X-rays; the emission center also matches within 1.5″ between two images. Given this agreement and the higher angular resolution ($\sim0\overset{″}{.}5$) of Chandra, we refer to the best-fitting position of the X-ray emission center in table 6 as the center of RCS J2319+0038 in the rest of this paper. The intrinsic X-ray luminosity within 15″ and 150″ from the center is $L_{\rm X} = (2.17 \pm 0.09) \times 10^{44}\ h_{70}^{-2}$ erg s^{-1} and $(4.42 \pm 0.30) \times 10^{44}\ h_{70}^{-2}$ erg s^{-1}, respectively, at $E_{\rm obs} = 0.4$–7.0 keV. Further comparison by means of a three-dimensional gas model will be discussed in subsections 4.1 and 4.3.

Figure 3 also shows that the centroid of the ACT SZE map of RCS J2319+0038 is offset from the centers of the ALMA and Chandra images by $\sim30″$

(230 h_{70}^{-1} kpc). We will discuss the possible origin of this offset in subsection 4.5.

We plot in figure 5 azimuthally averaged intensity profiles around the cluster center in four quadrants with position angles of 315°–45° (north), 45°–135° (east), 135°–225° (south), and 225°–315° (west). The statistical error in each bin is computed using equation (1) of Kitayama et al. (2016).

Figures 3 and 5 suggest that the ICM is disturbed near the center of RCS J2319+0038. The SZE signal tends to be stronger in the south and in the west of the center; the significance of departures from the azimuthal average is at $\sim2\sigma$ (see subsection 4.2). At $\theta \gtrsim 20″$, elongation in the east–west direction becomes more obvious. The X-ray emission peak is also offset from the cluster center, defined by fitting the global emission profile, by $\sim4″$ or $\sim32\ h_{70}^{-1}$ kpc.

3.2.2 HSC J0947−0119
Figure 4 shows the deconvolved ALMA image of HSC J0947−0119 after the compact sources listed in table 4 have been removed. As with the case of RCS J2319+0038, the results of an elliptical Gaussian fit are listed in table 5 and azimuthally averaged intensity profiles in four quadrants are plotted in figure 5.

The SZE signal of HSC J0947−0119 tends to be stronger and more extended than that of RCS J2319+0038, with a mean size of $\sim45″$ FWHM and an axis ratio of 0.66 ± 0.06 (table 5). The integrated flux density within 45″ from the position shown in table 5 is -3.66 ± 0.11 mJy. For reference, the flux inferred from the elliptical Gaussian fit is -4.12 ± 0.24 mJy.

The best-fitting center of the ALMA image ($9^{\rm h}47^{\rm m}58\overset{\rm s}{.}74$, $-1°19′58\overset{″}{.}37$) is 8″ north-east of the centroid position of the ACT image ($9^{\rm h}47^{\rm m}58\overset{\rm s}{.}30$, $-1°20′02\overset{″}{.}80$) and
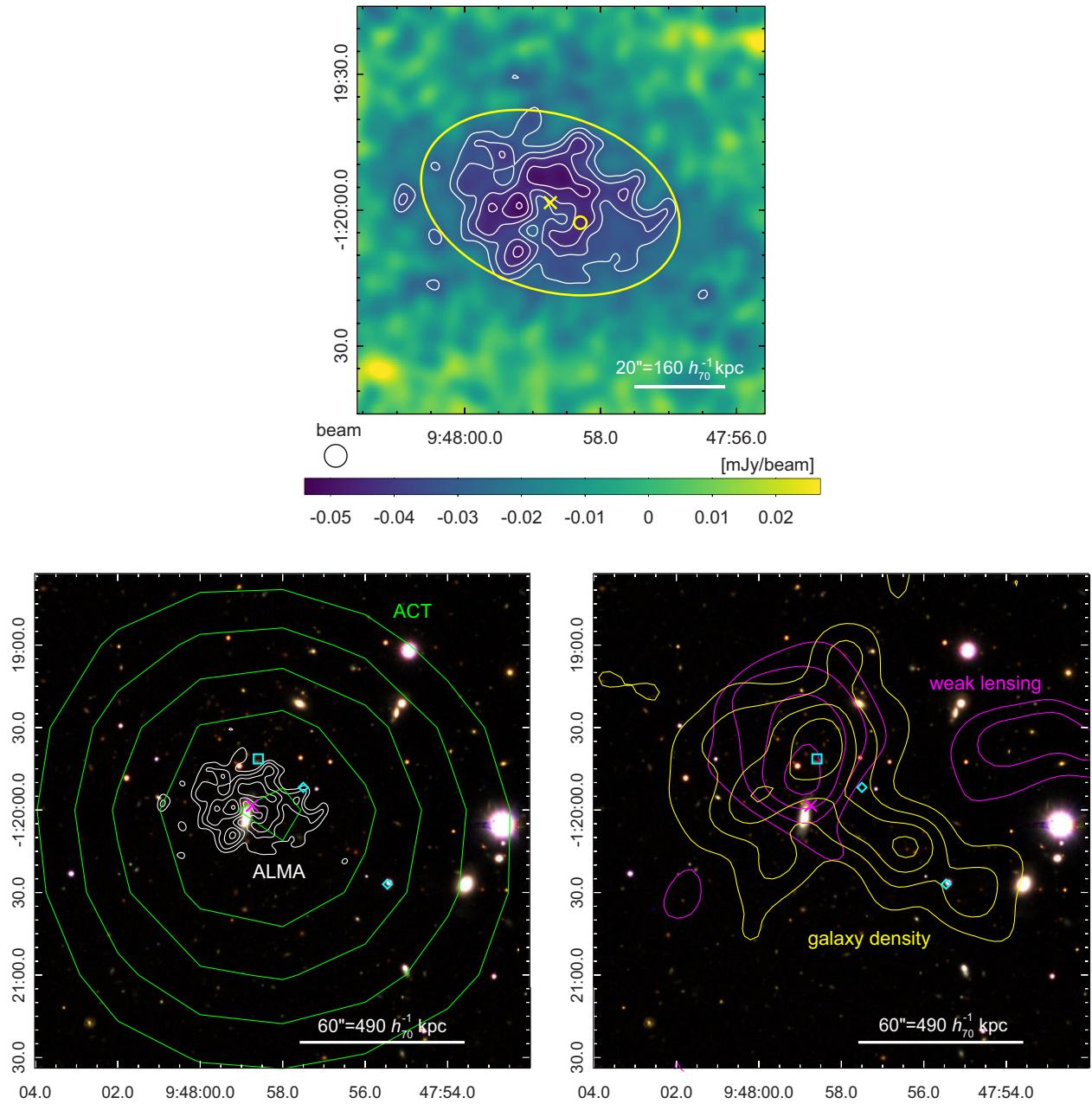
Fig. 4. Multi-wavelength view of HSC J0947−0119 at $z = 1.11$. Top: Deconvolved ALMA image at 92 GHz smoothed to have a beam size of 5″ FWHM. Symbols indicate the centers of the SZE signal measured by ALMA (cross) and ACT (circle). The ellipse shows the FWHM location of the best-fitting elliptical Gaussian profile (table 5). Bottom left and bottom right: Wider-field HSC-SSP optical *riz*-color image with the ALMA SZE center marked by a cross. The positions of the BCG and the off-center sources (W1 and W2) are indicated by a box and diamonds, respectively. Wherever plotted, white contours show the significance levels of the ALMA SZE image (5–9σ in increments of 1$\sigma = 5.9\,\mu$Jy beam^{-1}), green contours the significance levels of the SZE map from the ACT DR5 cluster catalogue ($S/N = 4, 6, 8, 10$, and 12), yellow contours the surface density of probable member galaxies averaged by a Gaussian with 20″ FWHM (80%, 60%, 40%, 20% of the peak value), and magenta contours the projected weak lensing mass smoothed by a Gaussian with 30″ FWHM ($S/N = 1.5, 2, 2.5$, and 3).

represents reasonable agreement considering the angular resolution (FWHM ~ 1.4) and the significance ($S/N = 13.2$) of the ACT data (see also subsection 4.5). Given the lack of Chandra data for this cluster, we refer to the former position as the center of HSC J0947−0119 in the rest of this paper.

Figures 4 and 5 suggest that the ICM in HSC J0947−0119 is disturbed. The SZE signal tends to be stronger along the north-east and south-west directions across the emission center. As will be discussed in subsection 4.2, the statistical significance of disturbance is at 2–3σ, and tends to be larger in this cluster than RCS J2319+0038.
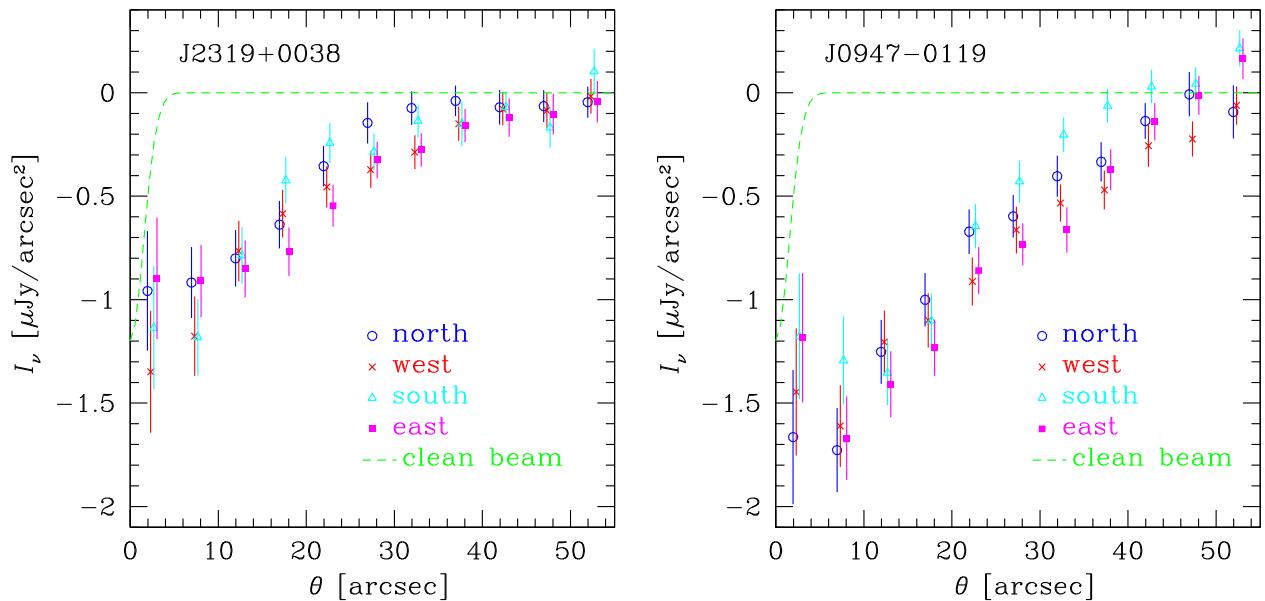
Fig. 5. Azimuthally averaged SZE intensity profiles RCS J2319+0038 (left) and HSC J0947−0119 (right) as a function of the projected distance from the cluster center in the four quadrants; north (circles), west (crosses), south (triangles), and east (squares). For clarity, symbols are slightly shifted horizontally. The dashed lines show the azimuthally averaged shapes of the synthesized beam.

3.3 Galaxy density and weak lensing mass

Figures 3 and 4 also show the HSC-SSP optical images of RCS J2319+0038 and HSC J0947−0119, respectively. The richness of these clusters is $N_{\mathrm{mem}} = 31.6$ and 67.5, respectively, where N_{mem} is the number of galaxies with stellar mass larger than $10^{10.2} M_\odot$ taking into account membership probability (see Oguri 2014 for a definition). The galaxies in both clusters show bimodal density peaks indicative of subcluster mergers, if they are not subject to a chance projection effect. The BCG lies in the main peak of galaxy density in each cluster.

The weak lensing signal is only marginally detected with the peak S/N of 2.8 and 3.2 for RCS J2319+0038 and HSC J0947−0119, respectively, after being smoothed by a Gaussian with 30″ FWHM. While the significance is low, the peak of the surface mass density is in agreement with the main peak of galaxy concentration. Assuming the NFW density profile (Navarro et al. 1996) and the mass–concentration relation of Diemer and Kravtsov (2015), the values of the characteristic mass, estimated from the weak lensing measurements, are $M_{500} = 3.6^{+4.6}_{-2.2} \times 10^{14} h_{70}^{-1} M_\odot$ and $2.6^{+3.2}_{-1.4} \times 10^{14} h_{70}^{-1} M_\odot$ for RCS J2319+0038 and HSC J0947−0119, respectively.[13] Note that the errors on M_{500} from weak lensing are very large for these distant clusters, owing to the limited number of background galaxies.

Figure 3 further indicates that the ALMA SZE and Chandra X-ray centers of RCS J2319+0038 coincide with the highest peak of galaxy density and the weak lensing mass. The BCG also lies within 1″ from the X-ray center. On the other hand, no concentration of the ICM is detected around the second peak of galaxy density, which lies at $\sim 40''$ east of the main peak. The ICM morphology is still elongated toward the second peak of galaxy density.

On the other hand, the SZE center of HSC J0947−0119 (figure 4) is persistently offset from the BCG and the main peak of galaxy density by about 17″ (140 h_{70}^{-1} kpc), suggesting the presence of a strong disturbance in this cluster. The ICM morphology is also elongated toward the second peak of galaxy density.

The above results imply that highly asymmetric galaxy distributions seen in optical images (figures 3 and 4) could be associated with relatively small values ($\lesssim 0.7$) of the axis ratio found for the ICM in both clusters (tables 5 and 6); average values of the axis ratio reported for massive clusters at low z are 0.8–0.9 (e.g., Kawahara 2010; Donahue et al. 2016).

4 Interpretation and implications

4.1 Imaging simulations

To quantify the missing flux of the ALMA data and to test the fidelity of the image reconstruction algorithm, we performed imaging simulations as follows.

---

[13] M_{500} is defined as the total mass enclosed in the radius R_{500}, within which the average matter density is 500 times the critical density of the Universe.

4.1.1 Method

We first specified the Compton y-parameter (i.e., projected electron pressure)

$$y(\vec{\theta}) = \int \sigma_{\mathrm{T}} n_{\mathrm{e}} \frac{k T_{\mathrm{e}}}{m_{\mathrm{e}} c^2} dl \qquad (3)$$

for each cluster in consideration, where σ_{T} is the Thomson cross section, k is the Boltzmann constant, m_{e} is the electron mass, c is the speed of light, and l denotes the physical length along the line of sight toward the sky position $\vec{\theta}$. Details of the models on n_{e} and T_{e} will be described in sub-subsection 4.1.2.

Input model images of the SZE were created from the above Compton y-parameter map separately at four spectral windows centered at 85, 87, 97, and 99 GHz with an effective bandwidth of 1.875 GHz each. A relativistic correction to the SZE intensity by Itoh and Nozawa (2004) was taken into account.

Visibility data were then produced using the CASA task *simobserve* including both instrumental and atmospheric thermal noise in each spectral window; this procedure was repeated 10 times adopting different noise seeds. The pointing directions, the array configuration, the hour angle, the total effective integration time, and the average precipitable water vapor were set to match those of each executing block of real observations for each cluster.

Finally, the mock visibility was deconvolved in the same way as the real data as described in subsection 2.1. For reference, we also performed "noise-only" runs in which the input SZE signal is set to zero. We have checked that the RMS levels of dirty maps created from such noise-only runs are consistent with the observed values in table 2. To take into account any bias in producing an image at a single frequency from the data taken over finite bandwidths, the simulation outputs are compared with an input model evaluated at the central frequency 92 GHz.

4.1.2 Input models

The model Compton y-parameter map of RCS J2319+0038 was constructed from the available X-ray data as follows. Fitting the 0.4–7.0 keV spectrum within $45''$ from the cluster center yielded the average electron temperature of $kT_{\mathrm{e}} = 5.90^{+0.79}_{-0.62}$ keV. Assuming that the gas is isothermal,[14]

---

[14] Our subsequent analysis is insensitive to this simplification. We checked that adopting a mean temperature profile for high-redshift clusters (McDonald et al. 2014) in the input model would change the value of c_1 in table 7 only within its error range. We will also show in subsection 4.4 that a weak temperature gradient is inferred from the joint analysis of the SZE and the X-ray data of RCS J2319+0038, whereas the gas density profile still follows equation (4).

a triaxial electron density profile consistent with an elliptical β model specified by equations (1) and (2) is

$$n_{\mathrm{e}}(\vec{r}) = n_{\mathrm{e}0} \left[1 + \frac{\bar{\theta}^2 + (\phi/\eta)^2}{\theta_{\mathrm{c}}^2} \right]^{-\frac{3}{2}\beta}, \qquad (4)$$

where $n_{\mathrm{e}0}$ is the central electron density, ϕ denotes the line-of-sight angular displacement between the three-dimensional position $\vec{r}$ and the cluster center (i.e., physical distance divided by the angular diameter distance to the cluster d_{A}), $\bar{\theta}$ is the mean angular radius on the sky as in equations (1) and (2), and η is the elongation factor along the line of sight. In other words, we assumed that the electron density profile has the axis ratio of

$$\sqrt{q} : \frac{1}{\sqrt{q}} : \eta \qquad (5)$$

where the first axis corresponds to $\bar{x}$ in equation (2) and the third axis is effectively along the line of sight; we neglected the inclination of the third axis from the line of sight, given the lack of data to constrain it. Adopting the fitted values of S_0, β, θ_{c}, q, and ψ from table 6 as well as $kT_{\mathrm{e}} = 5.90$ keV, we obtained $n_{\mathrm{e}0} = 1.43 \times 10^{-2} h_{70}^{1/2} \eta^{-1/2}$ cm^{-3}. Integrating the product of n_{e} and kT_{e} over the line of sight gives a Compton y-parameter map with the peak value of $y_{\mathrm{peak}} = 1.1 \times 10^{-4} h_{70}^{-1/2} \eta^{1/2}$. To specify the absolute value of the model intensity in the simulations, we assumed fiducially $h_{70}/\eta = 1$ to obtain $y_{\mathrm{peak}} = 1.1 \times 10^{-4}$; we will discuss the impact of varying h_{70}/η in subsection 4.3. To take into account uncertainties of this model parametrization, we will also examine the cases in which the overall normalization of the y-parameter is doubled or halved, i.e., $y_{\mathrm{peak}} = 2.2 \times 10^{-4}$ and 0.55×10^{-4}. We will show in subsections 4.2 and 4.3 that the case with $y_{\mathrm{peak}} = 1.1 \times 10^{-4}$ indeed agrees well with the observed ALMA data.

Given the lack of X-ray data for HSC J0947−0119, we used the average pressure profile measured from a statistical sample of X-ray clusters at $0.6 < z < 1.2$ by McDonald et al. (2014). We also assumed a triaxial gas profile consistent with the axis ratio and the position angle observed on the sky for this cluster (table 5). As with RCS J2319+0038, the axis ratio was assumed to be given by equation (5). As discussed in subsections 4.2 and 4.3, the observed ALMA data are well reproduced by this profile with $M_{500} = 5.7 \times 10^{14} M_{\odot}$ assuming $h_{70} = 1$ and $\eta = 1$. We hence adopted this profile for the present simulations and estimated the mean temperature to be $kT_{\mathrm{e}} = 9.4$ keV using the scaling relation of Reichert et al. (2011). The inferred peak value of the y-parameter is $y_{\mathrm{peak}} = 1.5 \times 10^{-4}$. The sensitivity of the result to the y-parameter map is examined by considering limiting cases where the overall map normalization

is doubled or halved (i.e., $y_{\rm peak} = 3.0 \times 10^{-4}$ and 0.75×10^{-4}).

4.1.3 Missing flux correction using simulation results

Figures 6 and 7 compare arbitrarily chosen realizations of the simulated images and the input models for RCS J2319+0038 and HSC J0947−0119, respectively. The azimuthal average of all realizations is shown in figure 8. The simulated images show similar amplitude and spatial extension to the real data plotted in figures 3 and 4 for $y_{\rm peak} = 1.1 \times 10^{-4}$ (RCS J2319+0038) and $y_{\rm peak} = 1.5 \times 10^{-4}$ (HSC J0947−0119), respectively.

As noted in Kitayama et al. (2016, 2020), the following linear relation holds on average for the simulated ALMA images:

$$I_\nu^{\rm out}(\vec{\theta}) = c_1 I_\nu^{\rm in}(\vec{\theta}) + c_0, \tag{6}$$

where $I_\nu^{\rm out}$ and $I_\nu^{\rm in}$ are respectively the intensities of output and input images at the same sky position $\vec{\theta}$. This equation relates the object's observed to intrinsic intensity and is used in subsections 4.3 and 4.4 to correct for the missing flux. To obtain c_1 and c_0 in equation (6), a set of data $(I_\nu^{\rm in}, I_\nu^{\rm out})$ was created for each sky position in each simulated image and then binned in descending order of $I_\nu^{\rm in}$. Each bin contains at least 1000 pixel data after accumulating 10 realizations for each adopted value of $y_{\rm peak}$. The mean and the standard deviation of $I_\nu^{\rm out}$ in each bin are plotted against $I_\nu^{\rm in}$ in figures 9 and 10. These figures indicate that equation (6) holds well and c_1 is insensitive to the adopted value of $y_{\rm peak}$ (i.e., the overall normalization of the emission); c_1 depends primarily on the shape and the gradient of the emission as well as the observing conditions (e.g., the *uv* coverage).

Table 7 lists the fitted values of c_0 and c_1, assuming that c_1 is common among different values of $y_{\rm peak}$ for each cluster. The obtained value of c_1 is close to unity but takes a smaller value for HSC J0947−0119, whose y-parameter profile is shallower than RCS J2319+0038 (figure 12). The specific value of c_0 will not affect our real data analysis as it will be eliminated in equation (7) described below.

Figures 6–8 further illustrate that the simulated images are in agreement with the input models once corrected by equation (6), as described above. The RMS values at $\theta < 45''$ in figures 6d, 6g, 7d, and 7 g are 6.2, 5.9, 5.7, and 6.3 μJy beam^{-1}, respectively, and fully consistent with noise.

The above results imply that the relative intensity with respect to some reference point $\vec{\theta}_{\rm ref}$ follows

$$I_\nu^{\rm out}(\vec{\theta}) - I_\nu^{\rm out}(\vec{\theta}_{\rm ref}) = c_1 \left[I_\nu^{\rm in}(\vec{\theta}) - I_\nu^{\rm in}(\vec{\theta}_{\rm ref}) \right] \tag{7}$$

nearly independently of the underlying value of $y_{\rm peak}$. The coefficient c_1 denotes how much of the intrinsic intensity is retained on average in the deconvolved image for each cluster. In the rest of this paper, we refer to the conversion from $I_\nu^{\rm out}(\vec{\theta}) - I_\nu^{\rm out}(\vec{\theta}_{\rm ref})$ to $I_\nu^{\rm in}(\vec{\theta}) - I_\nu^{\rm in}(\vec{\theta}_{\rm ref})$ using the best-fitting values of c_1 from table 7 as the "missing flux correction." We will apply this correction to the real data taking off-center positions as $\vec{\theta}_{\rm ref}$; specifically, the reference points are taken at the mean radius $\bar{\theta} = 35''$ from the cluster center, which lies at the envelope of the emission profiles from real data (figure 5) and simulation outputs (figure 8).

4.1.4 Systematic errors

We estimated systematic errors associated with the above missing flux correction as follows. The errors of $I_\nu^{\rm out}$ plotted in figures 9 and 10 are dominated by statistical ones; each bin contains more than 1000 pixel data (i.e., 100 per realization). The systematic deviation from equation (6) apart from such statistical errors is represented by the RMS deviation of the mean values of $(I_\nu^{\rm in}, I_\nu^{\rm out})$ from the best-fitting result: $\Delta I_\nu^{\rm in} = 0.021\,\mu$Jy arcsec^{-2} and 0.029 μJy arcsec^{-2} for RCS J2319+0038 and HSC J0947−0119, respectively. We regard $\sqrt{2}$ times this value (i.e., $\Delta I_\nu^{\rm in} = 0.030\,\mu$Jy arcsec^{-2} and 0.042 μJy arcsec^{-2} for RCS J2319+0038 and HSC J0947−0119, respectively) as the 1σ systematic uncertainty in the difference $I_\nu^{\rm in}(\vec{\theta}) - I_\nu^{\rm in}(\vec{\theta}_{\rm ref})$ recovered using equation (7).

We also examined if the subtraction of compact sources as described in subsection 3.1 affects the measurements of the SZE by adding sources C1 and C2 (table 3) to the simulations with $y_{\rm peak} = 1.1 \times 10^{-4}$ for RCS J2319+0038; the other sources are irrelevant to the measured SZE profiles. Repeating the simulations 10 times while varying the noise seeds, we found that the errors associated with the subtraction of C1 and C2 are fully statistical with no identifiable systematic effects on $I_\nu^{\rm out}$. At arbitrary positions in the cluster, we take the difference of $I_\nu^{\rm out}$ with respect to the point-source-free run with the same noise seed, regard its RMS value over the 10 realizations as an additional error in $I_\nu^{\rm out}$ due to the source subtraction, and add it to the errors of the measured SZE profiles in subsections 4.3 and 4.4.

Table 8 summarizes the systematic errors mentioned above, together with those included in the subsequent analysis.

4.2 Residual SZE images

Figure 11 shows residual images after the elliptical models described in subsection 4.1 are subtracted from the real ALMA images in figures 3 and 4. The subtracted models are essentially the same as those plotted in figures 6b and 7b;
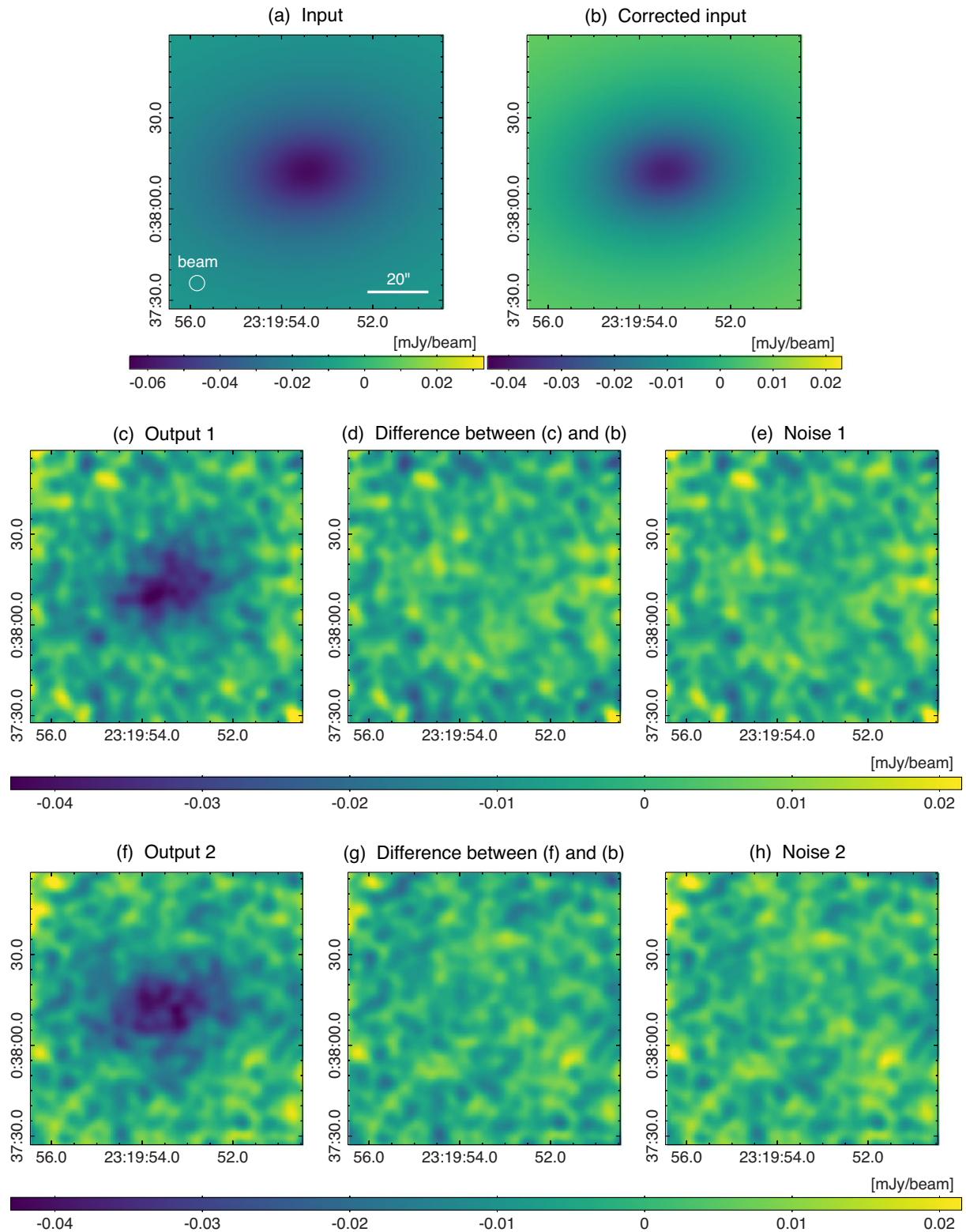
Fig. 6. Mock images of RCS J2319+0038 at 92 GHz with $y_{\text{peak}} = 1.1 \times 10^{-4}$. All the images have been smoothed to 5″ FWHM. (a) Input model. (b) Input model to which the correction encoded by equation (6) has been applied. (c) Simulation output including noise shown in panel (e). (d) Difference between panels (c) and (b). (e) Noise-only output for the run shown in panel (c). (f) Same as panel (c) but with a different noise realization shown in panel (h). (g) Difference between panels (f) and (b). (h) Noise-only output for the run shown in panel (f).
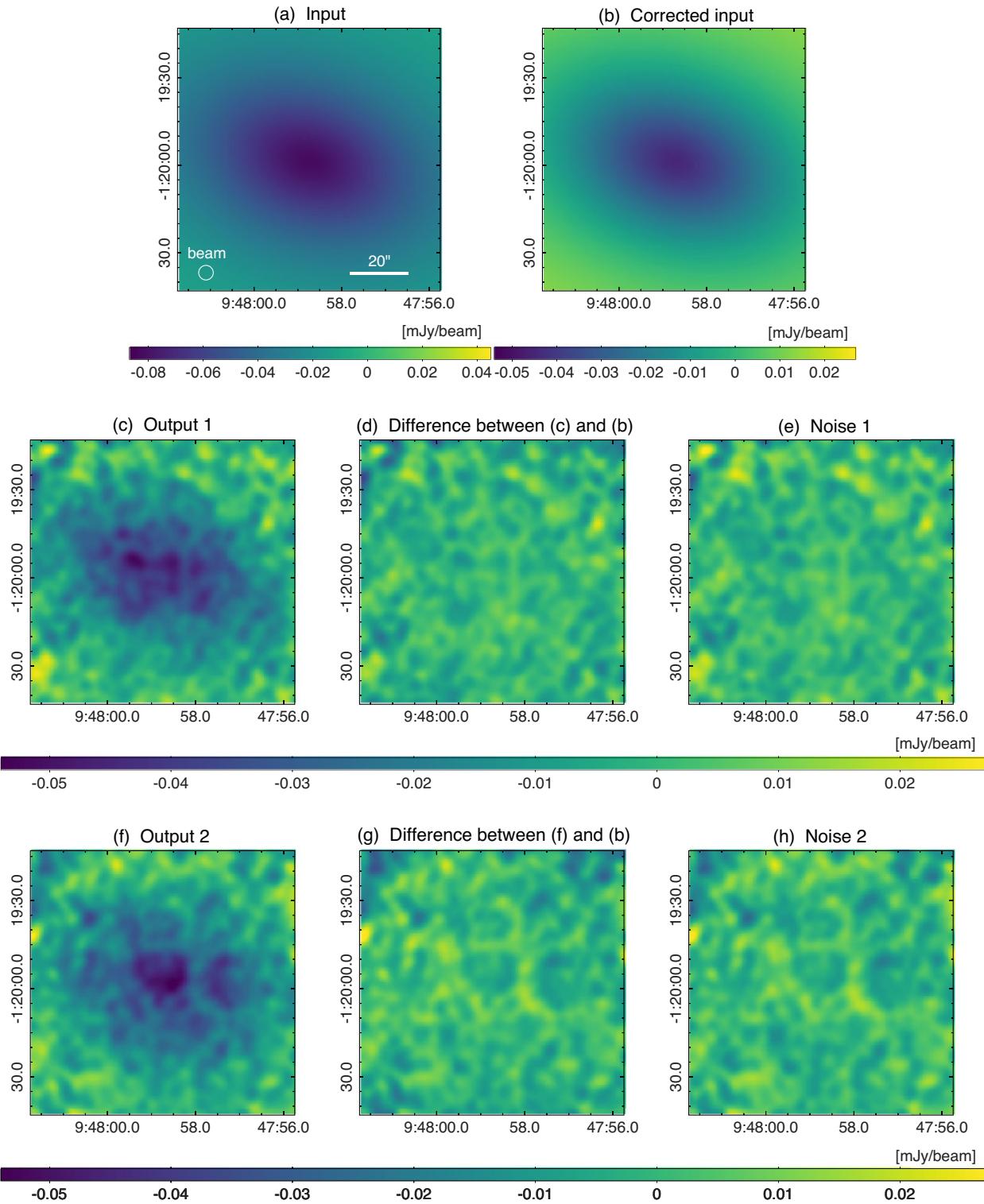
Fig. 7. Same as figure 6, except for showing mock images of HSC J0947−0119 with $y_{\mathrm{peak}} = 1.5 \times 10^{-4}$.

the intrinsic intensity has been corrected by equation (6) and smoothed to 5″ FWHM.

The residual images exhibit moderate (2–3σ) levels of deviations, which should comprise real departures from symmetry and noise. The RMS value of the residuals for HSC J0947−0119, 6.8 μJy beam^{-1}, is slightly larger than that for RCS J2319+0038, 6.5 μJy beam^{-1}. Apart from these deviations, the overall morphology of the real ALMA image is well reproduced by the elliptical model for each cluster.
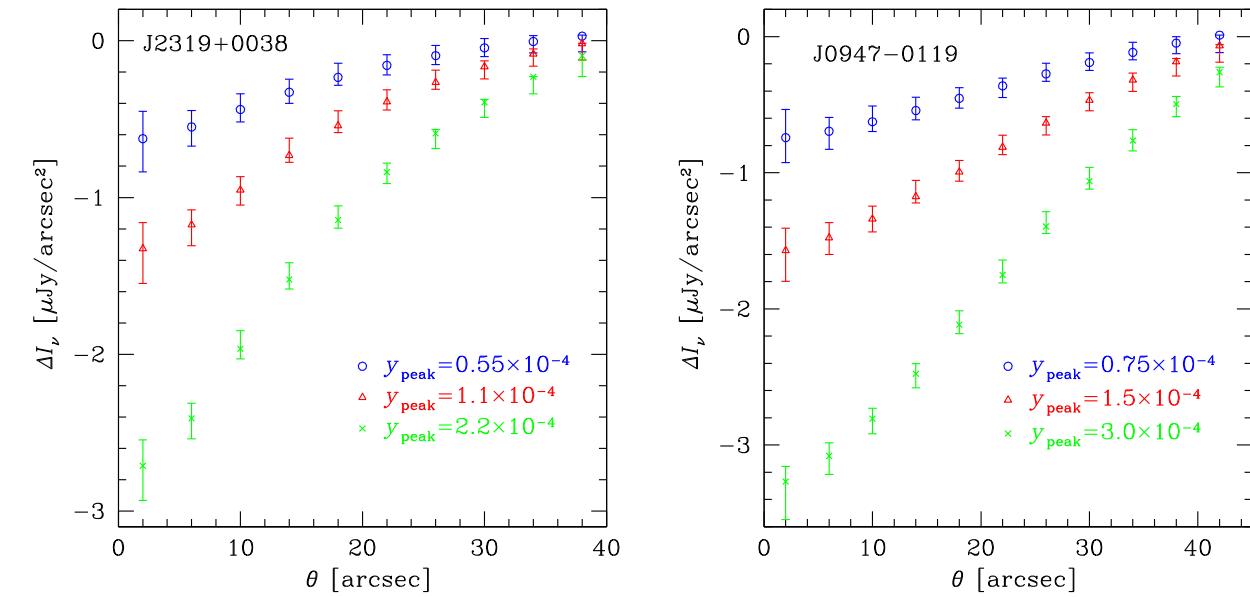
Fig. 8. Results of imaging simulations for RCS J2319+0038 (left) and HSC J0947−0119 (right). Error bars show azimuthally averaged intensity profiles from the simulations. Symbols show the same quantity from the input model to which the correction by equation (6) has been applied for each value of y_{peak} as indicated in the figure.
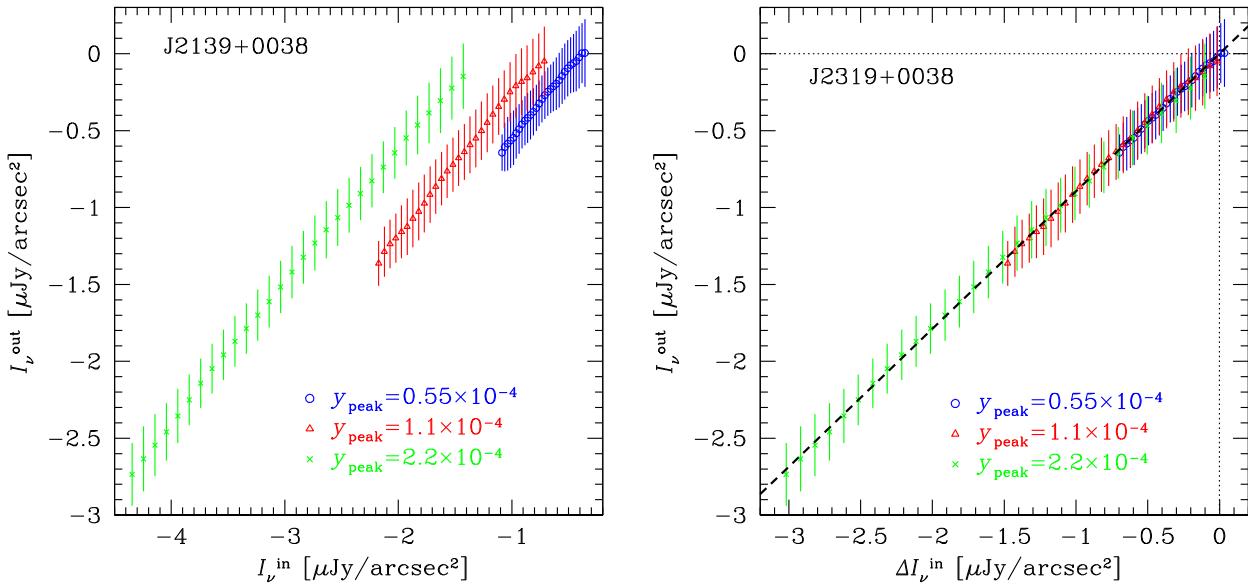
Fig. 9. Left: Relation between the output intensity and the input intensity at 92 GHz from the imaging simulations for RCS J2319+0038. Error bars and symbols denote the standard deviation and the mean, respectively, in each bin for $y_{peak} = 0.55 \times 10^{-4}$ (circles), 1.1×10^{-4} (triangles), and 2.2×10^{-4} (crosses). Right: Same as the left panel, except that the fitted value of c_0/c_1 in equation (6) has been added to I_ν^{in} to give a zero intercept in each case. The thick dashed line shows the best fitting relation with $c_1 = 0.89$ for this cluster (table 7).

4.3 Inner pressure profiles

The SZE images provide a direct probe of integrated electron pressure, i.e., the Compton y-parameter. We used the results of subsection 4.1 to reconstruct the Compton y-parameter profile as follows.

4.3.1 Method

The observed intensity was averaged over elliptical bins to take into account the elongated morphology of the clusters; the axis ratio and the position angle were fixed at the best-fitting values listed in tables 6 and 5 for
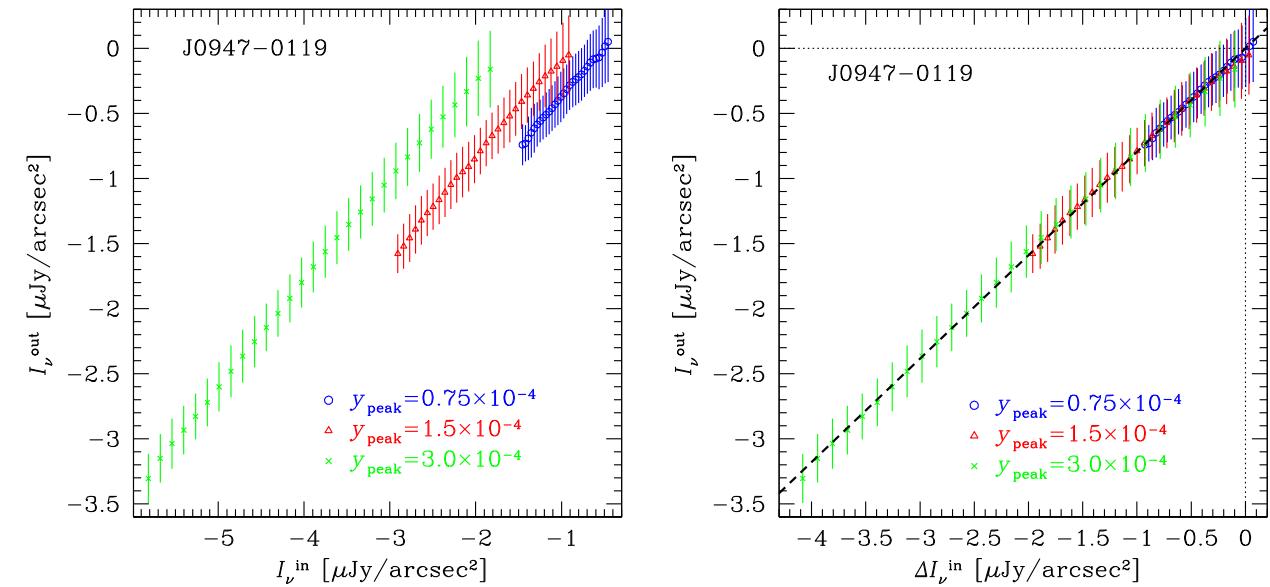
Fig. 10. Similar to figure 9 but showing the results for HSC J0947−0119. The thick dashed line shows the best fitting relation with $c_1 = 0.79$ for this cluster (table 7).

Table 7. Coefficients of the linear relation (6) from imaging simulations.*

Cluster	y_{peak} [10^{-4}]	c_1	c_0 [μJy arcsec^{-2}]
	0.55	0.89 ± 0.03	0.35 ± 0.04
RCS J2319+0038	1.1	0.89 ± 0.03	0.62 ± 0.06
	2.2	0.89 ± 0.03	1.19 ± 0.11
	0.75	0.79 ± 0.03	0.42 ± 0.05
HSC J0947−0119	1.5	0.79 ± 0.03	0.75 ± 0.07
	3.0	0.79 ± 0.03	1.38 ± 0.12

*The coefficient c_1 is assumed to be common for each cluster.

RCS J2319+0038 and HSC J0947−0119, respectively. The bins are geometrically spaced with the innermost bin at $0'' < \bar{\theta} < 4''$ and the bin width increasing by a factor of 1.1, so that the statistical error in the final y-parameter profile is less than about 20% in each bin (an increasing bin width alleviates the decreasing S/N with radius).

The intrinsic SZE intensity at 92 GHz was then computed for each bin using equation (7) and taking the seventh bin containing $\bar{\theta} = 35''$ (centered at $\bar{\theta} = 34''.4$) as the reference points ($\vec{\theta}_{ref}$). The systematic errors associated with the missing flux correction ($\Delta I_{\nu}^{in} = 0.030\,\mu$Jy arcsec^{-2} and $0.042\,\mu$Jy arcsec^{-2} for RCS J2319+0038 and HSC J0947−0119, respectively, estimated in sub-subsection 4.1.4) and the absolute calibration uncertainty of ALMA (6%; Kitayama et al. 2016) were added in quadrature to the statistical error in each bin. For RCS J2319+0038, the error from the source subtraction (sub-subsection 4.1.4, table 8), estimated as 0.117 and $0.023\,\mu$Jy arcsec^{-2} for the innermost and the second innermost bins, respectively, was also added in quadrature.

Finally, the intrinsic SZE intensity is proportional to the Compton y-parameter times the temperature-dependent relativistic correction factor c_{rel}, defined as the ratio between the true SZE intensity and the SZE intensity in the non-relativistic limit. For the range of temperatures considered in this paper, $3 < kT < 10$ keV, c_{rel} is in the range $0.94 < c_{rel} < 0.98$ at 92 GHz (e.g., Itoh & Nozawa 2004). To eliminate the dependence of the data points on the temperature, c_{rel} is used for correcting the model predictions and not the data in sub-subsection 4.3.2.

### 4.3.2 Reconstructed y-parameter profile

Figure 12 compares the Compton y-parameter profiles obtained with various model predictions. By construction, the model predictions, not the data points presented, are influenced by the relativistic correction via the assumed temperature and the values of h_{70} and η, introduced in equation (4). All the model predictions are smoothed to the same beam size and averaged over the same radial bins as the data in the analysis; unbinned predictions are shown for display purposes only.

We first examine the isothermal β model inferred from the X-ray data of RCS J2319+0038: $kT = 5.90$ keV, $n_{e0} = 1.43 \times 10^{-2} h_{70}^{1/2} \eta^{-1/2}$ cm^{-3}, $\beta = 0.673$, and $r_c = 103\, h_{70}^{-1}$ kpc. The observed y-parameter profile of RCS J2319+0038 is consistent with this model and provides a useful limit on h_{70}/η. If h_{70}/η is varied as a free parameter, the best-fitting value is

$$\frac{h_{70}}{\eta} = 1.07^{+0.15}_{-0.12} \tag{8}$$

Table 8. List of systematic errors included in the analysis of subsections 4.3 and 4.4.

Error source	RCS J2319+0038	HSC J0947−0119
Missing flux correction	$0.030\,\mu\mathrm{Jy\,arcsec}^{-2}$	$0.042\,\mu\mathrm{Jy\,arcsec}^{-2}$
Point-source subtraction	$0.117\,\mu\mathrm{Jy\,arcsec}^{-2}$ $(0 < \bar{\theta} < 4'')$	—
	$0.023\,\mu\mathrm{Jy\,arcsec}^{-2}$ $(4'' < \bar{\theta} < 8\rlap{.}''4)$	—
	$0.021\,\mu\mathrm{Jy\,arcsec}^{-2}$ $(0 < \bar{\theta} < 10'')$	—
Flux calibration of ALMA at 92 GHz	6% of the SZE intensity	6% of the SZE intensity
Effective area of Chandra ACIS-S	4% of the X-ray intensity	—
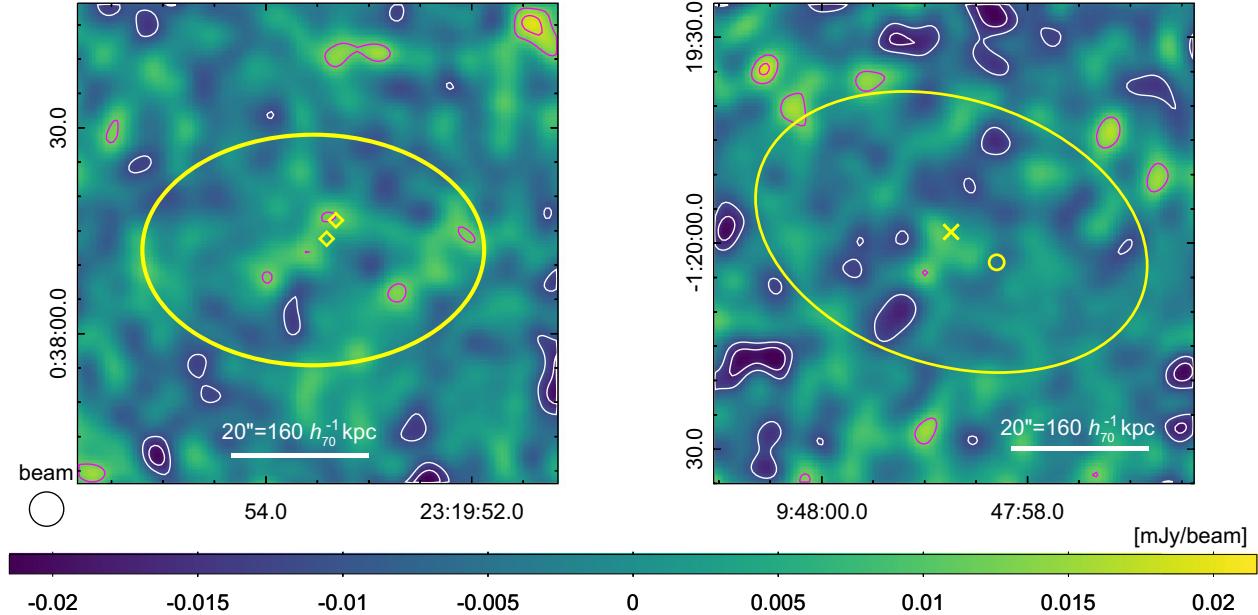
Fig. 11. Residual SZE images of RCS J2319+0038 (left) and HSC J0947−0119 (right) after the model used in the simulation described in subsection 4.1 is subtracted. Contours show 2, 3, and 4σ significance levels, for positive (magenta) or negative (white) values of residuals. The meanings of the ellipses and symbols are the same as in figures 3 and 4.

with the minimum χ^2 of 3.1 for five degrees of freedom (dof). Taking $h_{70}/\eta = 1$ as in the left panel of figure 12 gives $\chi^2 = 3.4$ and is in reasonable agreement with the data.

We also consider the generalized NFW pressure profile (Nagai et al. 2007) with model parameters obtained from a sample of X-ray selected clusters at $z < 0.2$ by Arnaud et al. (2010) or SZE selected clusters at $0.6 < z < 1.2$ by McDonald et al. (2014). Specifically, we used equation (13) of Arnaud et al. (2010) with the parameter values listed in table 5 of McDonald et al. (2014) for either "cool-core," "non-cool-core," or "all" clusters in each sample and allowed the characteristic mass M_{500} to vary. The relativistic correction was computed for the temperature specified by M_{500} and z from the scaling relation of Reichert et al. (2011). The SZE intensity predicted from the generalized NFW pressure profile varies as $I_{SZ} \propto c_{\mathrm{rel}}(M_{500}h_{70})^{2/3+0.12}\,h_{70}^{1/2}\eta\,R_{500} \simeq M_{500}^{1.10}\,h_{70}^{0.60}\eta$, where $R_{500} \propto M_{500}^{1/3}h_{70}^{-2/3}$, $c_{\mathrm{rel}} \propto T_{\mathrm{e}}^{-0.03}$ for $3 < kT_{\mathrm{e}} < 10$ keV

at 92 GHz, and $M_{500}\,h_{70} \propto T_{\mathrm{e}}^{1.62}$ from equation (23) of Reichert et al. (2011). Fitting the observed SZE intensity hence gives approximately

$$M_{500} \propto h_{70}^{-0.55}\eta^{-0.91}. \tag{9}$$

With this variation in mind, we present the results with $h_{70} = 1$ and $\eta = 1$ in what follows.

Table 9 lists the values of M_{500} fitted to the observed y-parameter profile of each cluster. As representative cases, we plot in figure 12 the model predictions for M_{500} *fixed* at the best-fitting value for "non-cool-core clusters at $z < 0.2$" (top) or "all clusters at $0.6 < z < 1.2$" (bottom) as marked by an asterisk in table 9. Notice that the predictions for the other models, shown for reference, do *not* correspond to the overall best fit. The agreement between the model and data improves upon allowing M_{500} the freedom to vary.

The y-parameter profile of RCS J2319+0038 is consistent with the average pressure profiles at $0.6 < z < 1.2$ or a
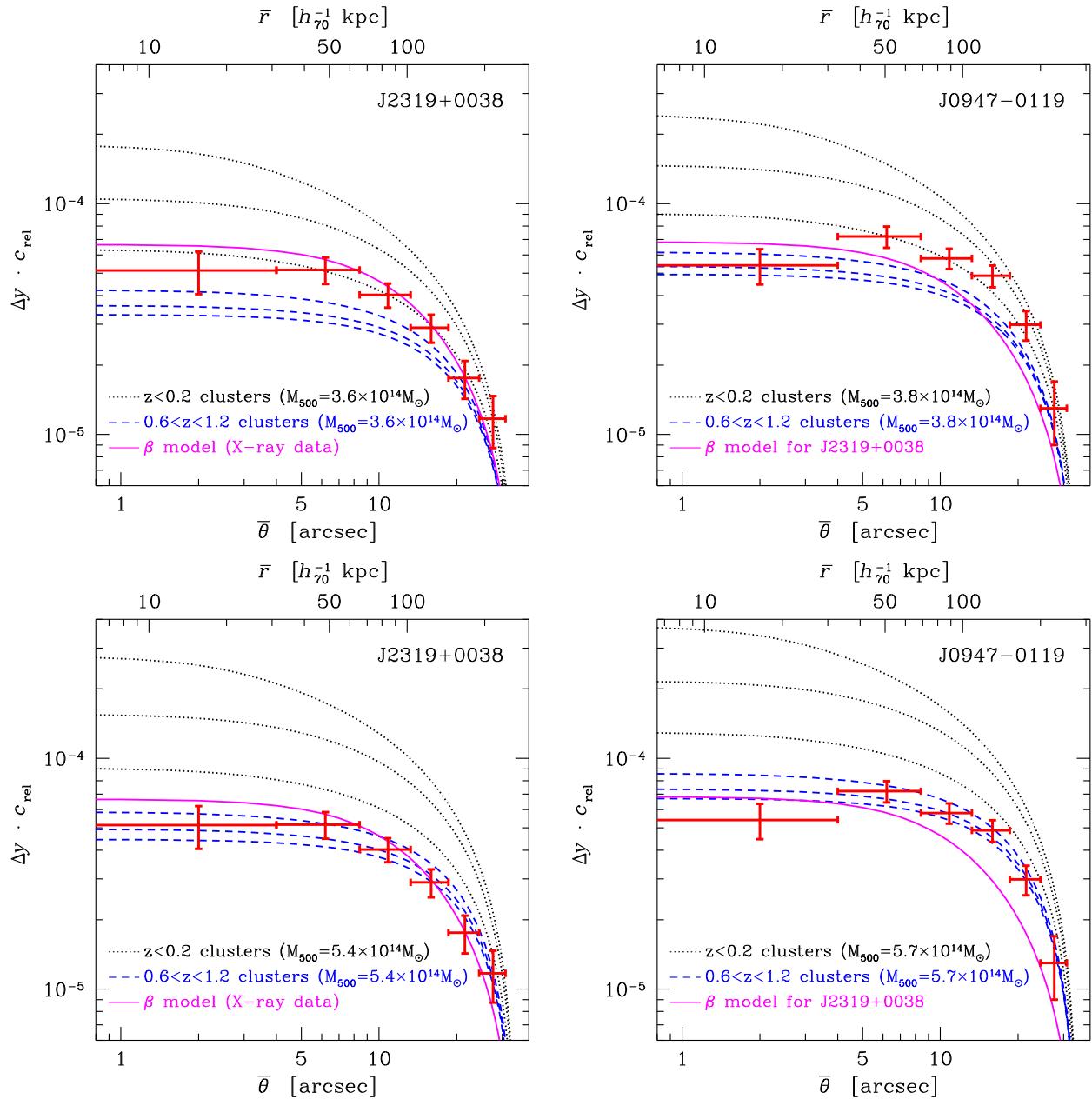
Fig. 12. Azimuthally averaged Compton y-parameter of RCS J2319+0038 (left) and HSC J0947−0119 (right) as a function of the mean angular radius $\bar{\theta}$, or the corresponding physical size $\bar{r} = \bar{\theta} d_A$. To eliminate the dependence of the data points (error bars) on the temperature, the y-parameter times the relativistic correction factor $c_{\rm rel}$ is plotted (see text for details). Overlaid are the expectations from the generalized NFW pressure profile for fixed M_{500} of X-ray selected clusters at $z < 0.2$ (dotted lines) by Arnaud et al. (2010) and SZE selected clusters at $0.6 < z < 1.2$ (dashed lines) by McDonald et al. (2014); three lines correspond to "cool-core," "all," and "non-cool-core" clusters in each sample from top to bottom. The value of M_{500} is fixed at $3.6 \times 10^{14} M_\odot$ (top left), $3.8 \times 10^{14} M_\odot$ (top right), $5.4 \times 10^{14} M_\odot$ (bottom left), and $5.7 \times 10^{14} M_\odot$ (bottom right) as marked by an asterisk in table 9. The solid line shows the β model profile inferred from the X-ray data of RCS J2319+0038. All the lines adopt $h_{70} = 1$ and $\eta = 1$. Both the data points and the expectations are relative to the positions at $\theta = 34\overset{''}{.}4$.

slightly steeper profile of non-cool-core clusters at $z < 0.2$. It is still much shallower than the average of cool-core clusters at $z < 0.2$. The fitted value of M_{500} for non-cool-core clusters at $z < 0.2$ or for cool-core clusters at $0.6 < z < 1.2$ is in reasonable agreement with $M_{500} = 4.01^{+0.38}_{-0.39} \times 10^{14} M_\odot$ inferred from the Chandra X-ray data of RCS J2319+0038

assuming hydrostatic equilibrium (Hicks et al. 2008), or with $M_{500} = 3.6^{+4.6}_{-2.2} \times 10^{14} M_\odot$ from our weak lensing analysis (subsection 3.3). For reference, Hilton et al. (2021) report the value[15] $M_{500} = 2.08^{+0.43}_{-0.36} \times 10^{14} M_\odot$ from the

---

[15] The mass quoted here is $M_{500c}^{\rm UPP}$ in Hilton et al. (2021).

Table 9. Results of fitting the y-parameter profile by generalized NFW models with $h_{70} = 1$ and $\eta = 1$.*

	RCS J2319+0038 at $z = 0.90$		HSC J0947−0119 at $z = 1.11$	
Assumed pressure profile	M_{500} [$10^{14} M_{\odot}$]	χ^2/dof	M_{500} [$10^{14} M_{\odot}$]	χ^2/dof
$z < 0.2$, cool-core	2.1 ± 0.1	11/5	2.1 ± 0.1	44/5
$z < 0.2$, all	2.5 ± 0.1	3.8/5	2.7 ± 0.1	24/5
$z < 0.2$, non-cool-core	*3.6 ± 0.2	1.3/5	*3.8 ± 0.2	11/5
$0.6 < z < 1.2$, cool-core	4.8 ± 0.3	2.3/5	5.0 ± 0.3	5.5/5
$0.6 < z < 1.2$, all	*5.4 ± 0.4	3.3/5	*5.7 ± 0.4	4.7/5
$0.6 < z < 1.2$, non-cool-core	6.0 ± 0.5	3.8/5	6.1 ± 0.4	4.5/5

*The fitted mass varies approximately as $M_{500} \propto h_{70}^{-0.55} \eta^{-0.91}$ (see text). The model profiles are sorted so that, for given M_{500} and z, the inner pressure gradient gets shallower in descending order. The values marked by an asterisk are used in figure 12.

ACT SZE data assuming the average pressure profile at $z < 0.2$ by Arnaud et al. (2010), whereas the value inferred from the mass–richness relation of Okabe et al. (2019) is $M_{500} \simeq 1.8 \times 10^{14} M_{\odot}$.

The y-parameter profile of HSC J0947−0119 appears to be even shallower than that of RCS J2319+0038 and is reproduced well by the average pressure profile of non-cool-core clusters at $0.6 < z < 1.2$. It is inconsistent with either average profiles of local clusters or the same β model as RCS J2319+0038 (χ^2/dof = 39/6). For reference, $M_{500} = 2.6^{+3.2}_{-1.4} \times 10^{14} M_{\odot}$ is inferred from our weak lensing analysis (subsection 3.3), $M_{500} = 4.05^{+0.64}_{-0.56} \times 10^{14} M_{\odot}$ from the ACT SZE data of HSC J0947−0119 assuming the average pressure profile at $z < 0.2$ (Hilton et al. 2021), and $M_{500} \simeq 5.7 \times 10^{14} M_{\odot}$ from the mass–richness relation of Okabe et al. (2019).

Note that the above y-parameter profiles are derived around the X-ray center of RCS J2319+0038 and the SZE center of HSC J0947−0119, given the lack of high-resolution X-ray data for the latter (subsection 3.2). The shallow pressure profile of HSC J0947−0119 could hence be due partly to a mismatch, if any, between the SZE center and the gas density peak, seen frequently in merging clusters. Future X-ray observations of HSC J0947−0119 will be useful for investigating this point further.

4.4 Deprojected electron temperature and density of RCS J2319+0038

Resolved SZE and X-ray brightness images of RCS J2319+0038 further allow us to constrain temperature and density profiles, thereby relaxing the isothermal approximation. The procedure is an extension of that described in Kitayama et al. (2020) to an ellipsoidal gas profile.

4.4.1 Method

The observed SZE or X-ray brightness was averaged over an elliptical annulus with the axis ratio and the position angle fixed at the best-fitting values in table 6. The bin size is $\Delta \bar{\theta} = 10''$ so that the statistical error in the brightness is less than 10% in each bin at $\bar{\theta} < 30''$. The intrinsic SZE intensity was computed for each bin using equation (7) and taking the fourth bin centered at $\bar{\theta} = 35''$ as the reference points ($\vec{\theta}_{\rm ref}$).

Systematic errors from the flux calibration of ALMA (6%, Kitayama et al. 2016), the missing flux correction of the SZE (0.030 μJy arcsec^{-2}, sub-subsection 4.1.4), and the effective area of Chandra ACIS-S (4%) were added in quadrature to the statistical error. The error from the source subtraction, estimated as 0.021 μJy arcsec^{-2} for the inner-most bin (sub-subsection 4.1.4, table 8), was also added in quadrature.

We then fitted the volume averaged brightness in each elliptical annulus (in 2D) of the SZE at $\bar{\theta} < 30''$ and of the 0.4–7.0 keV X-rays at $\bar{\theta} < 60''$ together varying the temperature and the density in each ellipsoidal shell (in 3D); the orientation of the axis was assumed to be the same as the triaxial β model described in sub-subsection 4.1.2. As the temperature at $\bar{\theta} > 30''$ ($\tilde{r} > 230$ kpc) cannot be constrained by the ALMA data, it was fixed at the projected mean value of 5.90 keV from the X-ray spectral analysis described in subsection 4.1.[16] For the SZE, we modeled incremental brightness relative to the bin centered at $\bar{\theta} = 35''$ taking account of the temperature-dependent relativistic correction in each ellipsoidal shell. The X-ray emissivity was computed by SPEX version 3.0.6.01 (Kaastra et al. 1996; J. S. Kaastra et al. 2020[17]).

From the reconstructed electron temperature and density, we evaluated entropy K and the radiative cooling time $t_{\rm cool}$ in each shell by

$$K = \frac{kT_e}{n_e^{2/3}}, \tag{10}$$

[16] We checked that the deprojected quantities at $\bar{\theta} < 20''$ (160 kpc) are insensitive to this assumption; they change within ±3% if the temperature at $\bar{\theta} > 30''$ is varied within the 1σ error range of $5.90^{+0.79}_{-0.62}$ keV.

[17] Kaastra, J. S., Raassen, A. J. J., de Plaa, J., & Gu, L. 2020, SPEX X-ray spectral fitting package ⟨https://doi.org/10.5281/zenodo.4384188⟩.

$$t_{\text{cool}} = \frac{3}{2} \frac{(n_{\text{e}} + n_{\text{H}} + n_{\text{He}})kT_{\text{e}}}{n_{\text{e}}n_{\text{H}}\Lambda_{\text{bol}}}, \tag{11}$$

where n_{H} and n_{He} are the number densities of hydrogen and helium atoms, respectively, and $n_{\text{e}}n_{\text{H}}\Lambda_{\text{bol}}$ denotes the bolometric luminosity per unit volume. We obtained Λ_{bol} by integrating the rest-frame X-ray emissivity from 0.1 eV to 1 MeV (e.g., Schure et al. 2009).

The quantities obtained by a joint SZE and X-ray analysis have different dependences on distance from those by the X-ray spectral analysis. The predicted SZE and X-ray intensities vary approximately as $I_{\text{SZ}} \propto n_{\text{e}}T_{\text{e}}^{\alpha_{\text{SZ}}} h_{70}^{-1}\eta$ and $I_{\text{X}} \propto n_{\text{e}}^2 T_{\text{e}}^{\alpha_{\text{X}}} h_{70}^{-1}\eta$, respectively, where $\alpha_{\text{SZ}} \simeq 0.97$ at 92 GHz and $\alpha_{\text{X}} \simeq 0.52$ at $E_{\text{obs}} = 0.4$–7.0 keV ($z = 0.90$), over the range $3 < kT_{\text{e}} < 10$ keV. Jointly fitting I_{SZ} and I_{X} gives

$$T_{\text{e}} \propto \left(\frac{h_{70}}{\eta}\right)^{\frac{1}{2\alpha_{\text{SZ}}-\alpha_{\text{X}}}} \simeq \left(\frac{h_{70}}{\eta}\right)^{0.70}, \tag{12}$$

$$n_{\text{e}} \propto \left(\frac{h_{70}}{\eta}\right)^{\frac{\alpha_{\text{SZ}}-\alpha_{\text{X}}}{2\alpha_{\text{SZ}}-\alpha_{\text{X}}}} \simeq \left(\frac{h_{70}}{\eta}\right)^{0.32}, \tag{13}$$

$$K \propto \left(\frac{h_{70}}{\eta}\right)^{\frac{3-2\alpha_{\text{SZ}}+2\alpha_{\text{X}}}{3(2\alpha_{\text{SZ}}-\alpha_{\text{X}})}} \simeq \left(\frac{h_{70}}{\eta}\right)^{0.49}, \tag{14}$$

$$t_{\text{cool}} \propto \left(\frac{h_{70}}{\eta}\right)^{\frac{1+\alpha_{\text{X}}-\alpha_{\text{SZ}}-\alpha_{\text{bol}}}{2\alpha_{\text{SZ}}-\alpha_{\text{X}}}} \simeq \left(\frac{h_{70}}{\eta}\right)^{0.09}, \tag{15}$$

where we have used $\Lambda_{\text{bol}} \propto T_{\text{e}}^{\alpha_{\text{bol}}}$ with $\alpha_{\text{bol}} \simeq 0.42$ for $3 < kT_{\text{e}} < 10$ keV in equation (15). We present the results with $h_{70}/\eta = 1$ in figure 13.

4.4.2 Deprojected profiles

Figure 13a shows the deprojected electron temperature profile of RCS J2319+0038. Also plotted for reference are the average profiles of cool-core and non-cool-core clusters at $0.6 < z < 1.2$ (McDonald et al. 2014). The results are consistent with the mean X-ray spectroscopic temperature of $kT_{\text{e}} = 5.90^{+0.79}_{-0.62}$ keV (sub-subsection 4.1.2). The measured temperatures tend to decrease moderately towards the center, in agreement with the average profile of high-redshift cool-core clusters. This is also consistent with the fact that the observed y-parameter profile of RCS J2319+0038 is better reproduced by a steeper pressure profile than the average of non-cool-core clusters at $0.6 < z < 1.2$ (figure 12 and table 9).

The associated electron density profile is plotted in figure 13b. It agrees well with the isothermal β model obtained solely from the X-ray data in sub-subsection 4.1.2, which provides a useful consistency test of the present technique. The electron density profile of RCS J2319+0038 with $n_{\text{e0}} \simeq 1.4 \times 10^{-2}$ cm^{-3} and $r_{\text{c}} \simeq 100$ kpc is shallower than the average of cool-core clusters at $0.2 < z < 1.9$ characterized by $n_{\text{e0}} > 1.5 \times 10^{-2}$ cm^{-3} and $r_{\text{c}} \simeq 20$–30 kpc (McDonald et al. 2017).

Figure 13c illustrates that the entropy decreases moderately to $\sim$80 keV cm^2 within the core ($\theta_{\text{c}} \simeq 13''$ or 100 kpc). Also plotted are a model $K \propto r^{1.2}$, which tends to give a lower limit to non-radiative clusters at $r \lesssim 0.5r_{500}$ (Voit et al. 2005), and a prediction $K \propto r^{1.4}$ for the steady-state cooling flow (Voit 2011); both profiles are normalized to match the data point in the outermost bin. The observed entropy profile shows a better agreement with $K \propto r^{1.2}$ than $K \propto r^{1.4}$, indicating that radiative cooling, if any, is modest in RCS J2319+0038.

Figure 13d further shows that the radiative cooling time in the core is about half the age of the Universe ($\sim$6 Gyr) at $z = 0.9$. The radial profile of the cooling time is represented approximately by a power law of $t_{\text{cool}} \propto r^{1.2}$. This is shallower than $t_{\text{cool}} \propto r^{1.7}$ obtained from a similar analysis for the Phoenix cluster at $z = 0.60$ (Kitayama et al. 2020), in which efficient radiative cooling is suggested.

4.5 Origin of the offset of the ACT SZE centroid of RCS J2319+0038

The centroid position of RCS J2319+0038 in the ACT SZE map is offset to the north-west direction by $\sim$30$''$ (230 h_{70}^{-1} kpc) from the centers of the ALMA SZE and the Chandra X-ray images (figure 3). We examined if this offset is due to the compact millimeter sources (table 3) unresolved in the ACT map, by means of cluster injection simulations similar to those done in Hilton et al. (2021).

We injected a model cluster and model sources to the real ACT map, re-ran filtering and cluster-detection procedures, and assessed the accuracy of the recovered cluster position. The compact sources listed in table 3 were found to be far too weak to produce the observed offset. The result is consistent with the fact that, according to figure 5 of Dicker et al. (2021), these sources would have changed the peak Compton y-parameter of RCS J2319+0038 in the ACT map [$\tilde{y}_0 = (6.1 \pm 1.2) \times 10^{-5}$ in Hilton et al. (2021)] by at most 4% for a spectral index of -0.7. Figure 4 of Hilton et al. (2021) further indicates that the accuracy of position recovery in the ACT SZE maps is sensitive to S/N and governed by the fluctuating cosmic microwave background (CMB). At the S/N of 5.2 for RCS J2319+0038, 22% of the injected clusters in the simulations are recovered at $>$30$''$ away from the position at which the cluster model was inserted. We thus conclude that the observed offset in the ACT SZE map of RCS J2319+0038 is statistically insignificant and likely due to the primary CMB fluctuations.
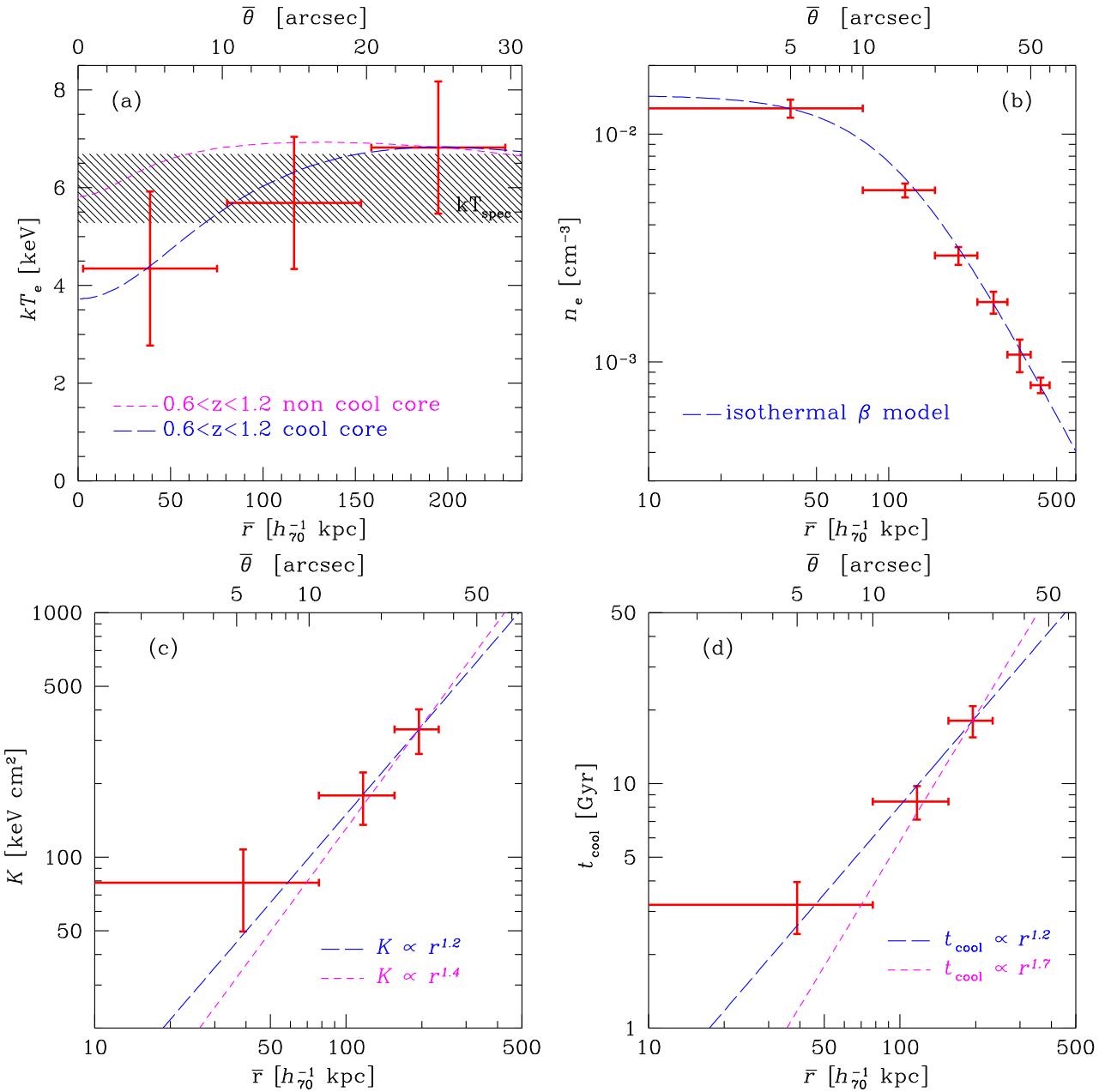
Fig. 13. Deprojected quantities of RCS J2319+0038 from SZE and X-ray images as a function of the mean radius $\bar{r}$ or the corresponding angular size $\bar{\theta} = \bar{r}/d_A$. (a) Electron temperature. Lines indicate the mean profiles of non-cool-core (short-dashed) and cool-core (long-dashed) clusters at $0.6 < z < 1.2$ by McDonald et al. (2014), both normalized to match the data point in the outermost bin. The shaded region shows the 1σ range inferred from the X-ray spectrum within $45''$ around the center of RCS J2319+0038. (b) Electron density. The dashed line indicates the isothermal β model (4) inferred from the X-ray data alone. (c) Entropy. Lines indicate the model profiles $K \propto r^{1.2}$ (long-dashed; Voit et al. 2005) and $K \propto r^{1.4}$ (short-dashed; Voit 2011), both normalized to match the data point in the outermost bin. (d) The radiative cooling time. Lines indicate the relations $t_{\rm cool} \propto r^{1.2}$ (long-dashed) and $t_{\rm cool} \propto r^{1.7}$ (short-dashed; Kitayama et al. 2020), both normalized to match the data point in the outermost bin. For definiteness, $h_{70} = 1$ and $\eta = 1$ are assumed; the data points vary approximately as $T_e \propto (\frac{h_{70}}{\eta})^{0.70}$, $n_e \propto (\frac{h_{70}}{\eta})^{0.32}$, $K \propto (\frac{h_{70}}{\eta})^{0.49}$, and $t_{\rm cool} \propto (\frac{h_{70}}{\eta})^{0.09}$ (see text).

We note that HSC J0947−0119 was detected by ACT with a higher S/N of 13.2 and exhibits agreement between the ACT and ALMA centroids (figure 4). This also supports the above interpretation that the position accuracy of the ACT SZE maps correlates with S/N.

5 Conclusions

We have presented ALMA Band 3 measurements of the thermal SZE toward two galaxy clusters at $z \sim 1$, RCS J2319+0038 and HSC J0947−0119, and performed joint analyses with available Chandra X-ray data, optical

data taken by Subaru/HSC, and wider-field SZE data by ACT. Taking into account departures from spherical symmetry, we have reconstructed the profiles of thermodynamic quantities non-parametrically. This is one of the first such measurements for an individual cluster at $z \gtrsim 0.9$.

In both clusters, the SZE is imaged at $5''$ resolution (corresponding to the physical scale of $\sim 40\ h_{70}^{-1}$ kpc) within $300\ h_{70}^{-1}$ kpc from the cluster center with the peak S/N exceeding 7. The overall morphology of the SZE signal is well described by an elliptical gas profile with axis ratio $\lesssim 0.7$, clearly differing from unity. The elongated morphology is probably associated with highly asymmetrical galaxy distributions found in these clusters. The inner pressure profile is consistent with the average of clusters at $0.6 < z < 1.2$ by McDonald et al. (2014) and is much shallower than that of local cool-core clusters by Arnaud et al. (2010).

Of the two clusters studied in this paper, high-quality X-ray data are available only for RCS J2319+0038. Both the centroid position and overall morphology of the ALMA SZE map are in agreement with those of the Chandra X-ray brightness image. We thus performed a non-parametric deprojection of electron temperature, density, entropy, and the radiative cooling time, combining SZE and X-ray images for RCS J2319+0038. Our results consistently indicate that RCS J2319+0038 hosts a weak cool core, where radiative cooling is less significant than in local cool cores. There are central radio sources as well as signs of subcluster mergers. We also suggest that the offset of the ACT SZE centroid position seen in this cluster (Hilton et al. 2021) is likely due to primary CMB fluctuations.

On the other hand, HSC J0947−0119 exhibits an even shallower pressure profile than RCS J2319+0038 and is more likely a non-cool-core cluster. The SZE centroid position is offset from the peaks of galaxy concentration by more than $140\ h_{70}^{-1}$ kpc, suggesting stronger impacts of mergers in this cluster than in RCS J2319+0038. No radio galaxies are found within $100\ h_{70}^{-1}$ kpc from either the SZE centroid or the peaks of galaxy concentration. Additional X-ray observations will be quite useful for exploring the nature of this cluster further.

We conclude that both of these distant clusters are at a very early stage of developing the cool cores typically found in clusters at lower redshifts. Our results also imply that high angular resolution SZE observations provide a unique probe of the thermodynamic structures of such clusters. We have developed an image domain analysis that allows for a non-parametric reconstruction of physical quantities from the ALMA data. An alternative and complementary approach is to perform model fitting in the visibility (uv) domain (e.g., Basu et al. 2016; Di Mascolo et al. 2019), which we plan to investigate in a future publication. We expect that the spectral and spatial ranges covered in future studies will be greatly enhanced by new facilities including the Band 1 receiver on ALMA (Huang et al. 2016), the Large Submillimeter Telescope (LST; Kawabe et al. 2016), and the Atacama Large Aperture Submillimeter/millimeter Telescope (AtLAST; Klaassen et al. 2019).

Acknowledgments

Maunakea, which has cultural, historical, and natural significance in Hawaii.

Appendix. Line emissions from compact sources

The ALMA Band 3 data presented in the present paper have a spectral resolution of 15.6 MHz and can be used for probing line emissions from galaxies in the fields of view. We find that sources W and W1 toward RCS J2319+0038 and HSC J0947−0119, respectively, host line emissions as listed in table 10. The position and the flux density are determined by fitting the visibility at >15 kλ over the frequency range shown in table 10 using the CASA task *uvmodelfit*. We also plot in figure 14 the spectra within a diameter of 7″ around the source position. Note that the continuum flux density of sources W and W1 in tables 3 and 4, respectively, are obtained excluding the frequency ranges listed in table 10. The short baselines (<15 kλ) are excluded in

the fit to eliminate possible contamination from the SZE signal. The line and continuum components so determined are subtracted from the visibility to construct the SZE maps shown in this paper. We have checked that there is no other line emission in the fields of view that would alter the detected SZE signal of RCS J2319+0038 and HSC J0947−0119.

The position of the line(s) at 97.8–98.2 GHz (W-b) agrees with that of source W in table 3 within 0.1″. On the other hand, the line at 85.0–85.3 GHz (W-a) lies at ∼2″ south-west of W-b and may be due to a different object from W and W-b. The line at 87.0–87.3 GHz (W1-a) lies at ∼1″ west of source W1.

It is difficult to determine the redshifts of the sources by a single emission line. For example, their ranges are $z = 1.3$–1.7 and 2.5–3.1 if the line is from CO(2–1) at 230.54 GHz and CO(3–2) at 345.80 GHz, respectively. The detailed nature of these sources is beyond the scope of this paper and will be investigated elsewhere.

Table 10. Line emissions in the fields of RCS J2319+0038 and HSC J0947−0119.*

Field	ID	ν [GHz]	RA (J2000.0)	Dec (J2000.0)	Integrated flux density [Jy km s^{-1}]
RCS J2319+0038	W-a	85.0–85.3	$23^h 19^m 49\overset{s}{.}58$	$+00°37'55\overset{''}{.}40$	0.76 ± 0.03
	W-b	97.8–98.2	$23^h 19^m 49\overset{s}{.}70$	$+00°37'56\overset{''}{.}47$	1.64 ± 0.03†
HSC J0947−0119	W1-a	87.0–87.3	$9^h 47^m 55\overset{s}{.}39$	$-1°20'26\overset{''}{.}66$	1.06 ± 0.02

*The integrated flux density is for the sum of line and continuum components over the frequency range shown.

†The flux density over the frequency gap at 98.028–98.060 GHz (figure 14 top right) is excluded. It is not relevant to the analysis of this paper.
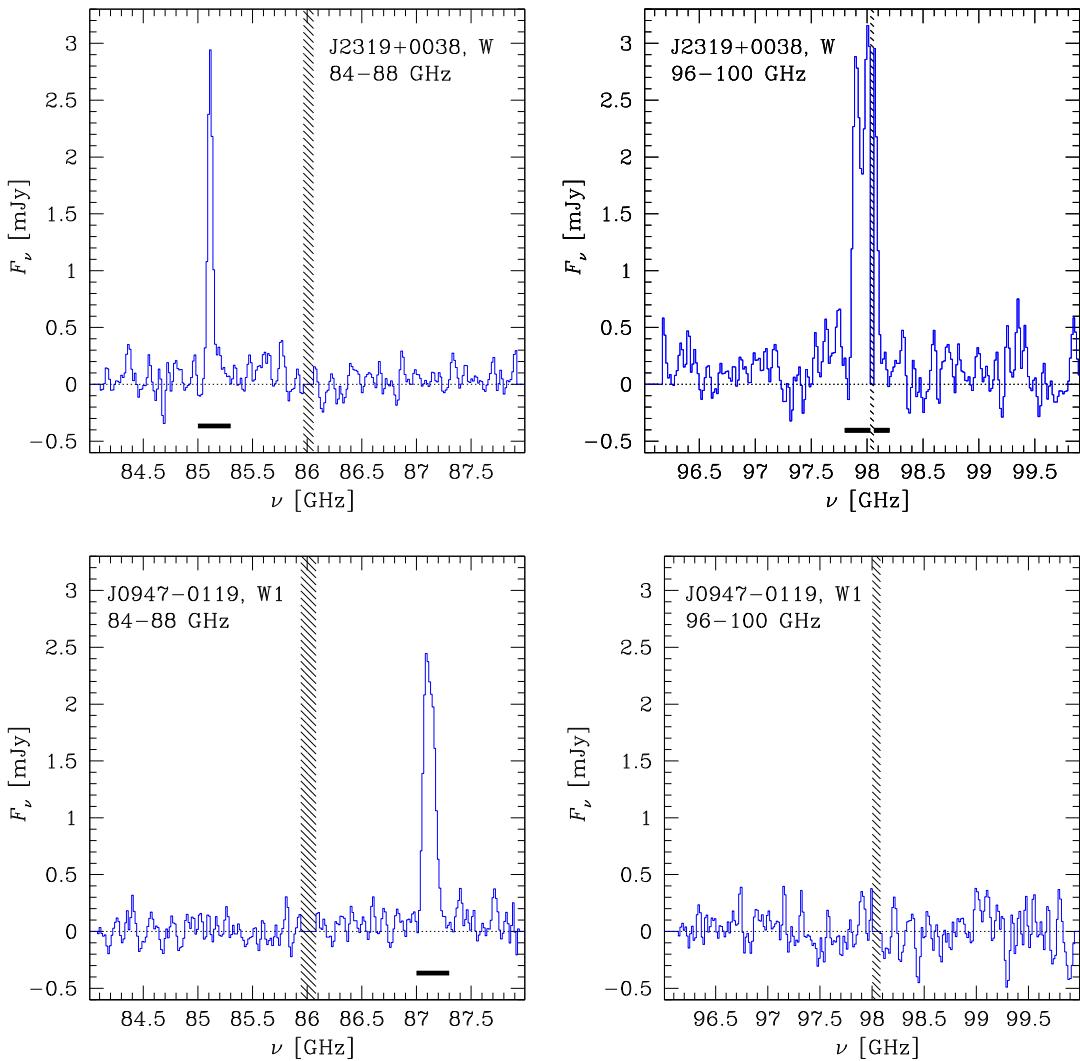
Fig. 14. Spectra of source W toward RCS J2319+0038 (top) and source W1 toward HSC J0947−0119 (bottom) against the observed frequencies at 84–88 (left) and 96–100 (right) GHz. Thick horizontal bars mark the frequency ranges over which the integrated flux density in table 10 is computed. Shaded regions show the frequency gaps over which the ALMA data are unavailable. Note that the data are not available at 88–96 GHz, either.

References

Abdurro'uf, et al. 2022, ApJS, 259, 35

Adam, R., et al. 2015, A&A, 576, A12

Adam, R., et al. 2018, A&A, 614, A118

Aihara, H., et al. 2018a, PASJ, 70, S4

Aihara, H., et al. 2018b, PASJ, 70, S8

Aihara, H., et al. 2019, PASJ, 71, 114

Aihara, H., et al. 2022, PASJ, 74, 247

Anders, E., & Grevesse, N. 1989, Geochim. Cosmochim. Acta, 53, 197

Andreon, S., et al. 2021, MNRAS, 505, 5896

Arnaud, K. A. 1996, ASP Conf. Ser., 101, 17

Arnaud, M., Pratt, G. W., Piffaretti, R., Böhringer, H., Croston, J. H., & Pointecouteau, E. 2010, A&A, 517, A92

Asplund, M., Grevesse, N., Sauval, A. J., & Scott, P. 2009, ARA&A, 47, 481

Bartalucci, I., Arnaud, M., Pratt, G. W., Démoclès, J., van der Burg, R. F. J., & Mazzotta, P. 2017, A&A, 598, A61

Basu, K., Sommer, M., Erler, J., Eckert, D., Vazza, F., Magnelli, B., Bertoldi, F., & Tozzi, P. 2016, ApJ, 829, L23

Bauer, F. E., Fabian, A. C., Sanders, J. S., Allen, S. W., & Johnstone, R. M. 2005, MNRAS, 359, 1481

Becker, R. H., White, R. L., & Helfand, D. J. 1995, ApJ, 450, 559

Blackburn, J. K. 1995, ASP Conf. Ser., 77, 367

Blackburn, J. K., Shaw, R. A., Payne, H. E., Hayes, J. J. E., & Heasarc 1999, Astrophysics Source Code Library, ascl:9912.002

Bleem, L. E., et al. 2015, ApJS, 216, 27

Böhringer, H., & Werner, N. 2010, A&AR, 18, 127

Bosch, J., et al. 2018, PASJ, 70, S5

Brodwin, M., McDonald, M., Gonzalez, A. H., Stanford, S. A., Eisenhardt, P. R., Stern, D., & Zeimann, G. R. 2016, ApJ, 817, 122

CASA Team 2022, PASP, 134, 114501

Cavaliere, A., & Lapi, A. 2013, Phys. Rep., 533, 69

Condon, J. J. 1997, PASP, 109, 166

Cornwell, T. J. 2008, IEEE J. Selected Topics in Signal Processing, 2, 793

Coupon, J., Czakon, N., Bosch, J., Komiyama, Y., Medezinski, E., Miyazaki, S., & Oguri, M. 2018, PASJ, 70, S7

Di Mascolo, L., et al. 2019, A&A, 628, A100

Di Mascolo, L., et al. 2020, A&A, 638, A70

Di Mascolo, L., et al. 2021, A&A, 650, A153

Dicker, S. R., et al. 2020, ApJ, 902, 144

Dicker, S. R., et al. 2021, MNRAS, 508, 2600

Diemer, B., & Kravtsov, A. V. 2015, ApJ, 799, 108

Doe, S., et al. 2007, ASP Conf. Ser., 376, 543

Donahue, M., et al. 2016, ApJ, 819, 36

Freeman, P., Doe, S., & Siemiginowska, A. 2001, Proc. SPIE, 4477, 76

Fruscione, A., et al. 2006, Proc. SPIE, 6270, 62701V

Furusawa, H., et al. 2018, PASJ, 70, S3

Ghirardini, V., et al. 2021, ApJ, 910, 14

Gilbank, D. G., Yee, H. K. C., Ellingson, E., Hicks, A. K., Gladders, M. D., Barrientos, L. F., & Keeney, B. 2008, ApJ, 677, L89

Gladders, M. D., & Yee, H. K. C. 2005, ApJS, 157, 1

Gobat, R., et al. 2019, A&A, 629, A104

Gordon, Y. A., et al. 2021, ApJS, 255, 30

Hasselfield, M., et al. 2013, J. Cosmology Astroparticle Phys., 1307, 008

HI4PI Collaboration 2016, A&A, 594, A116

Hicks, A. K., et al. 2008, ApJ, 680, 1022

Hilton, M., et al. 2018, ApJS, 235, 20

Hilton, M., et al. 2021, ApJS, 253, 3

Hincks, A. D., et al. 2010, ApJS, 191, 423

Hirata, C., & Seljak, U. 2003, MNRAS, 343, 459

Huang, Y. D. T., et al. 2016, Proc. SPIE, 9911, 99111V

Huang, S., et al. 2018, PASJ, 70, S6

Huang, N., et al. 2020, AJ, 159, 110

Itoh, N., & Nozawa, S. 2004, A&A, 417, 827

Kaastra, J. S., Mewe, R., & Nieuwenhuijzen, H. 1996, in UV and X-ray Spectroscopy of Astrophysical and Laboratory Plasmas, ed. K. Yamashita & T. Watanabe (Tokyo: Universal Academy Press), 411

Kawabe, R., Kohno, K., Tamura, Y., Takekoshi, T., Oshima, T., & Ishii, S. 2016, Proc. SPIE, 9906, 990626

Kawahara, H. 2010, ApJ, 719, 1926

Kawanomoto, S., et al. 2018, PASJ, 70, 66

Kitayama, T., et al. 2016, PASJ, 68, 88

Kitayama, T., et al. 2020, PASJ, 72, 33

Klaassen, P., et al. 2019, BAAS, 51, 58

Komiyama, Y., et al. 2018, PASJ, 70, S2

Korngut, P. M., et al. 2011, ApJ, 734, 10

Li, X., et al. 2022, PASJ, 74, 421

Mandelbaum, R., et al. 2018, PASJ, 70, S25

Mantz, A. B., Allen, S. W., Morris, R. G., Canning, R. E. A., Bayliss, M., Bleem, L. E., Floyd, B. T., & McDonald, M. 2020, MNRAS, 496, 1554

Marriage, T. A., et al. 2011, ApJ, 737, 61

Mason, B. S. 2020, arXiv:2006.06549

McDonald, M., et al. 2014, ApJ, 794, 67

McDonald, M., et al. 2017, ApJ, 843, 28

McMullin, J. P., Waters, B., Schiebel, D., Young, W., & Golap, K. 2007, ASP Conf. Ser., 376, 127

Medezinski, E., et al. 2018, PASJ, 70, 30

Miyazaki, S., et al. 2018, PASJ, 70, S1

Mroczkowski, T., et al. 2019, Space Sci. Rev., 215, 17

Naess, S., et al. 2020, J. Cosmology Astroparticle Phys., 2012, 046

Nagai, D., Kravtsov, A. V., & Vikhlinin, A. 2007, ApJ, 668, 1

NASA High Energy Astrophysics Science Archive Research Center (Heasarc) 2014, Astrophysics Source Code Library, ascl:1408.004

Navarro, J. F., Frenk, C. S., & White, S. D. M. 1996, ApJ, 462, 563

Oguri, M. 2014, MNRAS, 444, 147

Oguri, M., et al. 2018, PASJ, 70, S20

Okabe, N., et al. 2019, PASJ, 71, 79

Okabe, N., et al. 2021, MNRAS, 501, 1701

Peres, C. B., Fabian, A. C., Edge, A. C., Allen, S. W., Johnstone, R. M., & White, D. A. 1998, MNRAS, 298, 416

Planck Collaboration 2020, A&A, 641, A6

Refsdal, B. L., et al. 2009, in Proc. 8th Python in Science Conference, ed. G. Varoquaux et al. (SciPy Project), 51

Reichardt, C. L., et al. 2013, ApJ, 763, 127

Reichert, A., Böhringer, H., Fassbender, R., & Mühlegger, M. 2011, A&A, 535, A4

Rich, J. W., de Blok, W. J. G., Cornwell, T. J., Brinks, E., Walter, F., Bagetakos, I., & Kennicutt, R. C. J. 2008, AJ, 136, 2897

Sanders, J. S., Fabian, A. C., Russell, H. R., & Walker, S. A. 2018, MNRAS, 474, 1065

Santos, J. S., Tozzi, P., Rosati, P., Nonino, M., & Giovannini, G. 2012, A&A, 539, A105

Schure, K. M., Kosenko, D., Kaastra, J. S., Keppens, R., & Vink, J. 2009, A&A, 508, 751

Staniszewski, Z., et al. 2009, ApJ, 701, 32

Sunyaev, R. A., & Zeldovich, Y. B. 1970, Comments Astrophys. Space Phys., 2, 66

Sunyaev, R. A., & Zeldovich, Y. B. 1972, Comments Astrophys. Space Phys., 4, 173

Tanaka, M. 2015, ApJ, 801, 20

Tanaka, M., et al. 2018, PASJ, 70, S9

Tozzi, P., et al. 2015, ApJ, 799, 93

Vanderlinde, K., et al. 2010, ApJ, 722, 1180

Verde, L., Treu, T., & Riess, A. G. 2019, Nature Astron., 3, 891

Voit, G. M. 2011, ApJ, 740, 28

Voit, G. M., Kay, S. T., & Bryan, G. L. 2005, MNRAS, 364, 909

Williamson, R., et al. 2011, ApJ, 738, 139